Department of Physics and Astronomy; University of Canterbury
Private Bag 4800, Christchurch, New Zealand

Analysis of PSC Formation using Parcel Temperature Histories

Master of Science Thesis

Fraser Dennison

Supervisors:
Dr. Adrian McDonald
Dr. Simon Alexander

Abstract

Polar Stratospheric Clouds (PSCs) are composed of $HSO_4/HNO_3/H_2O$ aerosols called supercooled ternary solution (STS), solid nitric acid trihydrate (NAT) particles and ice particles. These clouds require the low temperatures found in the polar regions of the lower stratosphere to occur. PSCs are important due to the critical role they play in the destruction of ozone over the poles. The role of PSCs in ozone destruction has been understood since the 1980's however the mechanisms involved in PSC formation, particularly NAT formation, is still not well understood. Typically formation of PSCs in climate models is handled by using a temperature threshold as a proxy. A commonly used threshold is the equilibrium temperature for the existence of NAT, T_{NAT}; however when the area with temperatures below T_{NAT} are compared with observations of PSC it is found that this measure significantly over-estimates the abundance of PSC.

This research uses back trajectories stemming from the site of PSC observations to investigate the effect that the temperature history has on PSC formation. The trajectories are calculated using a simple Lagrangian model on an isentropic surface. The observational PSC data is obtained from the CALIOP (Cloud Aerosol Lidar with Orthogonal Polarization) instrument, which is from the CALIPSO (Could Aerosol Lidar and Infrared Pathfinder Satellite Observations) mission launched in 2006. The CALIOP data used in this research is taken from the June to September period from the years 2007-10 and for latitudes between -55° and -82°S, and totals in excess of 7 million individual measurement profiles, a four day back trajectory is calculated for each observation along the 450 K isentropic level. Temperature and wind data is from the MERRA (Modern Era Retrospective-analysis for Research and Applications) reanalysis and H_2O and HNO_3 concentrations (required for calculating equilibrium temperatures) are from Earth Observing System (EOS) Aura Microwave Limb Sounder (MLS) version 3.3.

It was found that different PSC types had different characteristics in their temperature histories. The mean temperature history associated with ice observations cooled by around 3 K over the previous 24 hours to slightly below the water ice frost point at the time of observation. However, in trajectories associated with the presence of NAT the temperature has on average stayed 4-5 K below T_{NAT} for the entire four days of the trajectory. Based on these findings and theories of PSC formation, a system for predicting PSC occurrence based on the temperature histories is proposed. This system provides a better approximation for the total extent of PSC occurrence than the T_{NAT} threshold. The average area covered by PSC on the 450 K level over the period examined as observed by CALIOP was 7.6 million km^2 while the area predicted by the temperature histories was 8.6 million km^2 as compared to 20.4 million km^2 with temperatures below T_{NAT}. The average geographical coverage of the different PSC types is reasonably well replicated by the temperature history classification; however, the ability to discriminate between different PSC types based on individual temperature histories is somewhat limited.

Acknowledgments

I would like to thank the following people for their help throughout production of this thesis:

- My supervisor Dr. Adrian McDonald for all his input, enthusiasm and feedback
- My supervisor Dr. Simon Alexander for providing the CALIOP data and some valuable feedback on my research
- Dr. Andrew Klekociuk for running the microphysical model

Contents

Chapter 1

Introduction

Polar Stratospheric Clouds (PSCs) play a critical role in the destruction of ozone at the poles. While this has been understood for many years, the mechanisms involved in the formation of PSCs are still not well understood. This lack of understanding results in the overestimation in the abundance of PSC in models when compared to PSC observations, for example Figure 1.1 shows the area covered by observed PSC over the Antarctic during 2007 (top panel) compared to the PSC area estimated by the common proxy used for PSC formation, the temperature threshold T_{NAT} (bottom panel); $\mathrm{T_{NAT}}$ is explained in section 2.2. In can be seen that PSC coverage is overestimated by a factor of 2.5 at times. This can lead to errors in predictions of ozone depletion in global climate models (GCMs). This work aims to find an empirical prescription which describes PSC formation which may be integrated into chemistry-climate models. In particular the temperature history of air parcels will be examined for their effect on PSC formation.

1.1 The Stratosphere

The stratosphere is the second layer of the atmosphere located between altitudes of 10 and 50 km. The stratosphere is characterized by increasing temperature with altitude (a positive lapse rate) whereas the adjacent troposphere (below) and mesosphere (above) have decreasing temperature with altitude as shown in Figure 1.2. It is this positive lapse rate in the stratosphere that acts against vertical motion of air parcels, making this layer stratified, hence the name. The tropopause and stratopause are the bounding regions between the stratosphere and the troposphere and mesosphere respectively, where the temperature remains approximately constant with changing altitude. The majority of Earth's ozone is located in the stratosphere as indicated in Figure 1.3.

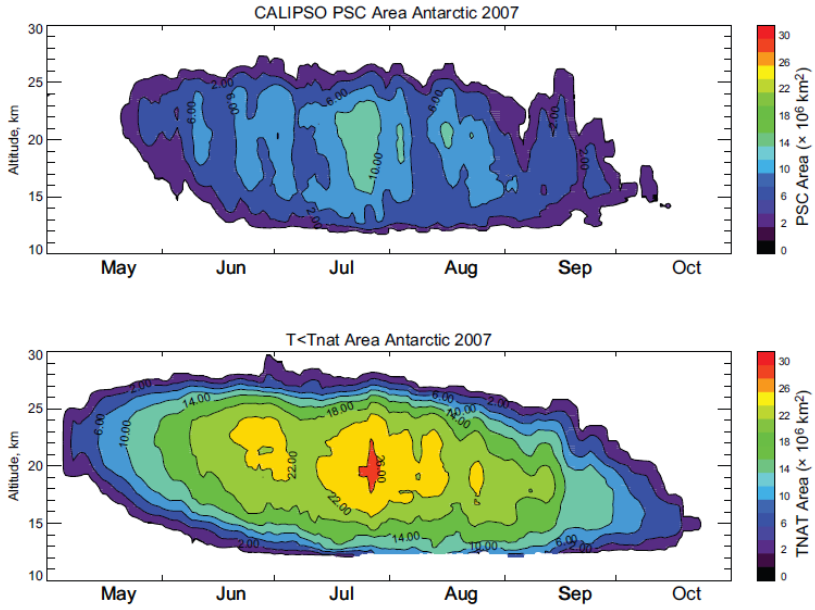

Figure 1.1: Observation of areal coverage of PSC (top) compared to the area with temperatures below T_{NAT} (bottom) over the Antarctic during 2007 (Source: WMO [2010])

1.2 PSC and Ozone Depletion

PSCs, as the name suggests, form in the polar lower stratosphere due to the cold temperatures found in that region. They are also known as nacreous cloud (from nacre, commonly known as mother of pearl) due to their characteristic colour and iridescence, an image of a PSC is shown in Figure 1.4. Remote sensing measurements traditionally divide PSC into three types; designated 1a, 1b and 2. These types are believed to be composed of $HSO_4/HNO_3/H_2O$ aerosols called supercooled ternary solution (STS), solid nitric acid trihydrate (NAT) particles and ice particles, respectively. More discussion of the PSC types can be found in chapter 2. The role of PSCs in ozone destruction was discovered by Solomon et al. [1986]. It was found that gas phase reactions were insufficient to account for the observed loss of ozone at the poles and that heterogeneous reactions occurring on the surface of PSC were required to explain the large magnitude of the ozone depletion.

Stratospheric ozone is important because it absorbs solar UV radiation in the 290-320 nm wavelength range. This radiation is harmful to humans; it increases the risk of skin cancer, cataracts and a suppressed immune system as well as damaging plant life, single cell organisms and aquatic ecosystems in cases of excessive exposure [WMO 2010]. Ozone loss over the Antarctic is therefore important as air depleted in ozone can occasionally be transported over populated regions such as New Zealand, South America and occasionally Australia [Ajtic et al. 2004]. Ozone is also a factor in the global climate, the absorption of solar radiation by ozone is the main factor determining the temperature in the stratosphere.

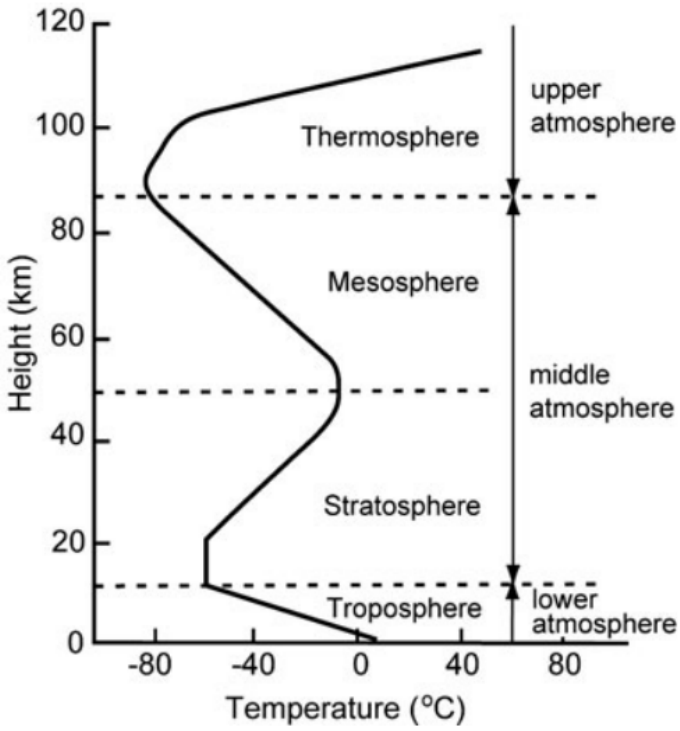

Figure 1.2: A schematic of the temperature structure of the atmosphere (Source: van Beek [2012])

Ozone is naturally produced in the stratosphere when molecular oxygen is split into two oxygen atoms by solar radiation with wavelength < 240 nm. The highly reactive oxygen atoms then combine with molecular oxygen to produce ozone. This set of reactions is summarized in equation 1.1.

$$\begin{aligned} O_2 + h\nu &\rightarrow 2O \\ 2[O + O_2 &\rightarrow O_3] \\ Net : 3O_2 + h\nu &\rightarrow 2O_3 \end{aligned} \tag{1.1}$$

Ozone is also naturally destroyed in the stratosphere via the reactions shown in equation 1.2. Ozone is broken into molecular oxygen and an oxygen atom by solar radiation with wavelength < 290 nm. The oxygen atom can then combine with another ozone molecule to produce two molecules of oxygen.

$$\begin{aligned} O_3 + h\nu &\rightarrow O_2 + O \\ O + O_3 &\rightarrow 2O_2 \\ Net : 2O_3 + h\nu &\rightarrow 3O_2 \end{aligned} \tag{1.2}$$

These reactions are known as the Chapman cycle [Chapman 1930]. The differing wavelengths in the production and destruction reactions are important as this results in the production and destruction occurring in different regions.

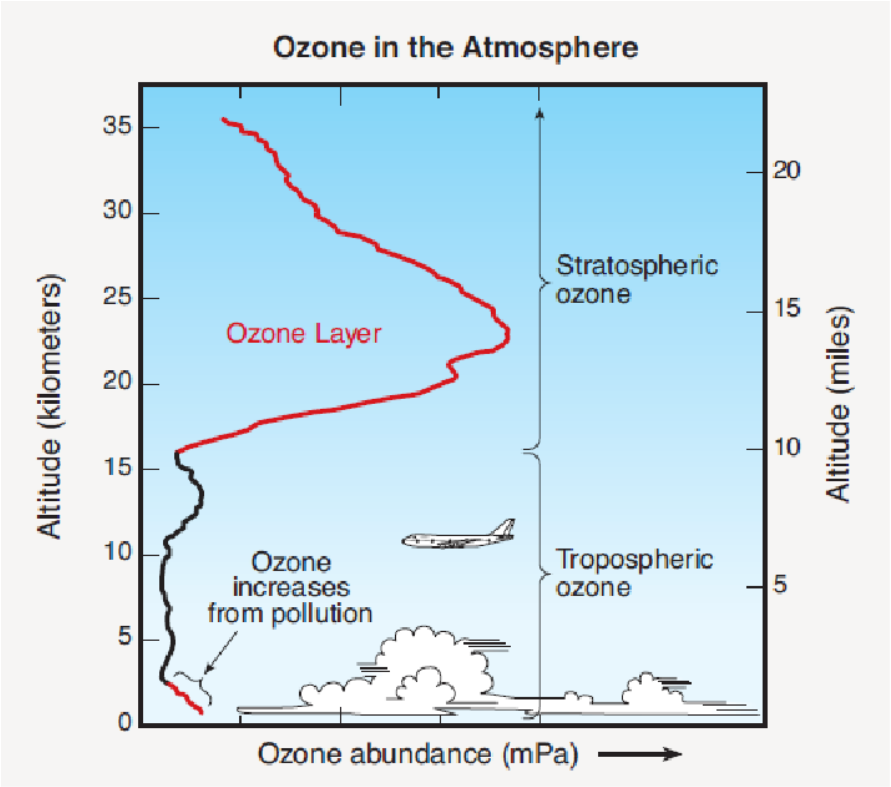

Figure 1.3: Ozone in the atmosphere (Source: WMO [2010])

In addition to the previous reaction, ozone is also destroyed by reactions with free radical catalysts. Ozone destroying free radicals include OH, NO_x, Cl, Br, ClO, and BrO and are represented by X in the following reaction:

$$\begin{aligned} X + O_3 &\rightarrow XO + O_2 \\ O_3 + h\nu &\rightarrow O_2 + O \\ XO + O &\rightarrow X + O_2 \\ Net : 2O_3 + h\nu &\rightarrow 3O_2 \end{aligned} \tag{1.3}$$

Man-made chlorofluorocarbons (CFCs) released into the troposphere during the latter half of the 20^{th} century form the reservoir species HCl, $ClONO_2$, HBr, $BrONO_2$, and HOBr when they break down in the stratosphere. Heterogeneous reactions on the surface of PSCs transform these reservoir species into species such as Cl_2, HOCl, and ClBr which are then photolysed into ozone destroying radicals when sunlight returns in the spring. The rate of one such heterogeneous reaction is shown as a function of temperature for different PSC constituents in Figure 1.5. Clearly the production of different PSC types plays a key role in the activation of the ozone depleting substances. Thus, identification of when different PSC types occur is a vital step in quantifying ozone destruction.

As well as providing the surface for the above reaction PSCs also aid in the destruction of ozone through denitrifcation [Drdla and Turco 1991; Khosrawi et al. 2011]. Denitrifcation is the process in which gaseous nitrogen is removed from the atmosphere in

Figure 1.4: An image of polar stratospheric cloud over Hut Point, Antarctica (Source: Masters [2005])

order to form NAT or absorbed by STS, this nitrogen would otherwise be used in the reaction that transforms free radicals back into reservoir species, for example in the reaction:

$$ClO + NO_2 \rightarrow ClONO_2 \tag{1.4}$$

In addition to nitrogen just being temporarily trapped in the PSC particle, permanent loss of nitrogen from the stratosphere can also occur when larger NAT particles (known as NAT rocks) sediment out of the stratosphere [Fueglistaler et al. 2002].

Another important aspect to ozone loss is the polar vortex. The polar vortex is a strong eastward stratospheric jet circling the Antarctic; an example of the wind field is illustrated in Figure 1.6. It is caused by steep latitudinal temperature gradients that are the result of continuous darkness in the polar region during winter. The vortex acts as barrier to mixing between polar and midlatitude regions. Ozone-poor air over the pole therefore cannot mix with ozone rich air from the midlatitudes and ozone destroying chemicals formed by PSCs are retained in the Antarctic stratosphere for long periods of time, which means that they are free to continuously destroy ozone via catalytic cycles linked to free chlorine and bromine.

The Antarctic ozone hole was first reported in 1985 by scientists at the British Antarctic Survey [Farman et al. 1985], measurements of Antarctic ozone show that the hole continued to grow through the 1980's and into the '90's. Figure 1.7 shows the evolution of the ozone destruction through to 2009 in the Arctic and Antarctic; in this figure the ozone hole is quantified as the October ozone poleward of 63° in Dobson units (DU; one DU is equal to a quantity of gas that would be 10 μm thick if brought to standard

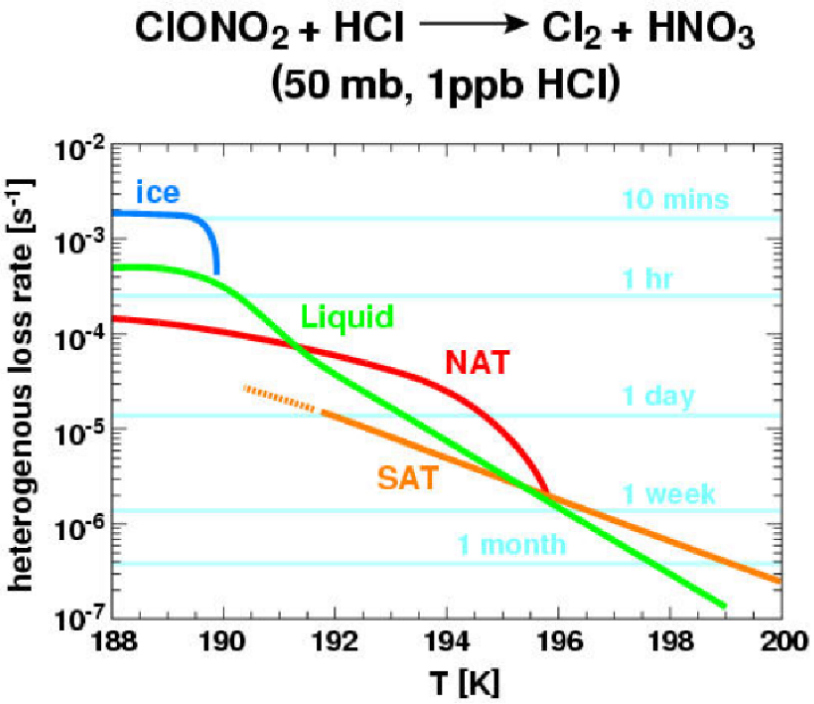

Figure 1.5: Heterogeneous chlorine activation rate of different PSC types (Source: Larsen [2000])

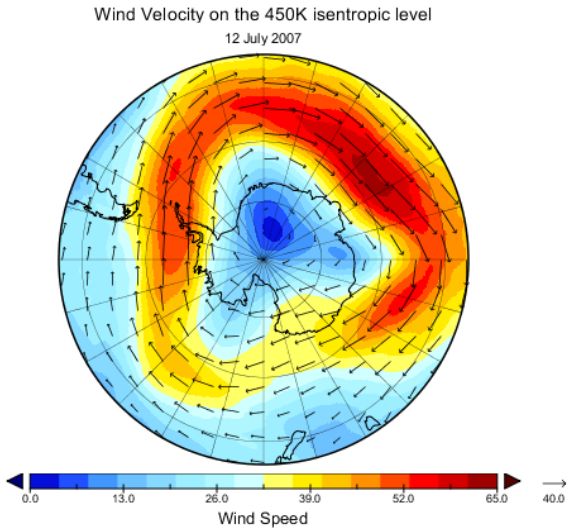

Figure 1.6: Wind field over the Antarctic showing the polar vortex

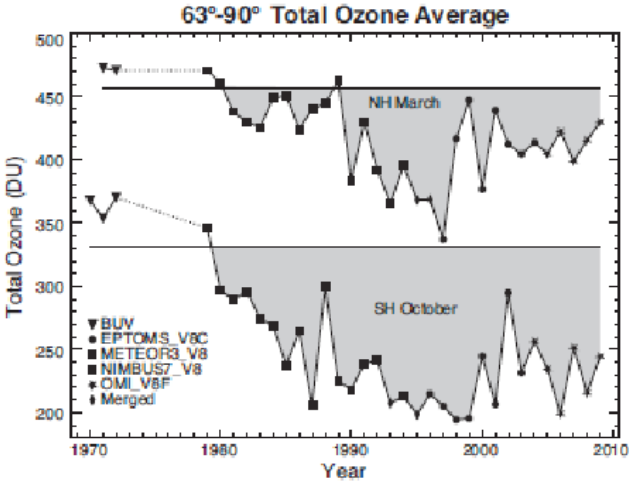

Figure 1.7: Evolution of the ozone losses in the Arctic and the Antarctic (Source: WMO [2010])

temperature and pressure). The gray area indicates the loss compared to the 1970-82 average; it can be see that the Antarctic has significantly larger ozone losses than the Arctic. As previously noted this is due to the strong Antarctic vortex as well as colder temperatures which are critical for PSC formation. As a result of the Montreal Protocol stratospheric chlorine has begun to decrease after peaking in the mid-nineties and subsequent recovery of stratospheric ozone is expected; eventually recovering to the 1980 level around the middle of this century WMO [2010].

1.3 PSC Detection

PSC particles were first measured using the solar occultation technique by the SAM II (Stratospheric Aerosol Measurement) instrument on board the Nimbus 7 satellite [McCormick et al. 1981, 1982]. Solar occultation is the technique wherein the attenuation of solar radiation through the atmospheric limb (a slice tangential to the Earth's surface) is measured. This method is limited in that measurements can only be taken when the satellite is in a position to observe a sunrise or sunset and the measurement is restricted to a vertical profile of one point on the horizon, the orbit of Nimbus 7 was such that about 14 of these measurement opportunities occur per day [McCormick et al. 1981]. However, these measurements were sufficient to allow McCormick et al. [1982] to observe a correlation between high extinction and low temperature. SAM II only measured the extinction at one wavelength (1.0μm); however subsequent instruments such as SAGE III (Stratospheric Aerosol and Gas Experiment) and POAM (Polar Ozone and Aerosol Measurement) III measured extinction at multiple wavelengths. Using the ratio of 603 and 1018 nm extinctions in the POAM dataset Strawa et al. [2002] was able to discriminate between type 1a and type 1b PSC. MIPAS (Michelson Interferometer for Passive Atmospheric Sounding) is another instrument used for detecting atmospheric

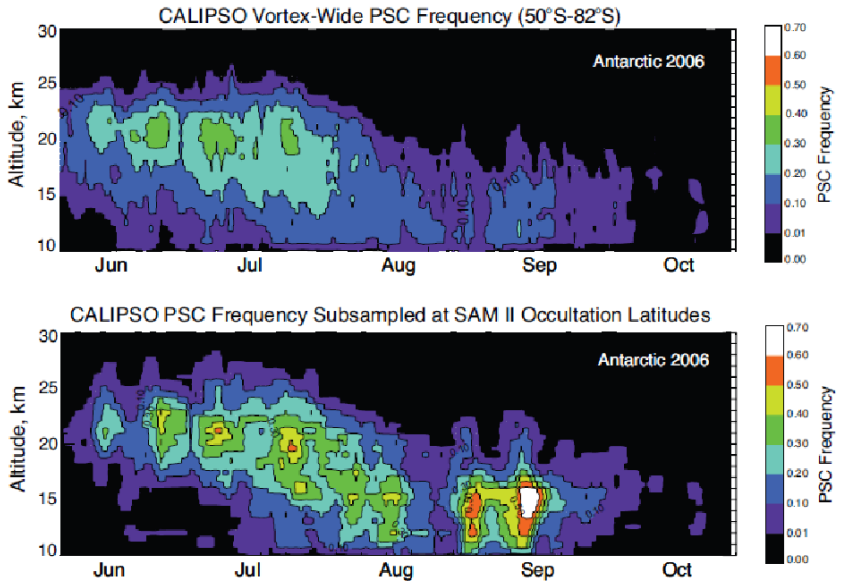

Figure 1.8: Comparison of PSC frequency calculated from CALIOP observation (top) and only CALIOP observations sub-sampled at locations of solar occultation measurement locations (Source: WMO [2010])

aerosols and gases; it has a spectral range of 4.5-15 μm [Burkert et al. 1983]. Using data from this instrument Höpfner et al. [2006] was able to separate PSCs into types 1a, 1b and 2.

Lidar (Light detection and ranging) is another method for acquiring measurements of PSC. Lidar works by pointing a beam of light in the direction of interest and measuring the intensity of the backscattered radiation; the distance to the cloud is determined by the amount of time it takes for the light to return. Early lidar measurements such those described by Stefanutti et al. [1991] and Adriani et al. [2004] were solely ground based, however PSC data for this study are derived from satellite based lidar measurements, specifically the CALIOP (Cloud Aerosol Lidar with Orthogonal Polarization) instrument from the CALIPSO (Could Aerosol Lidar and Infrared Pathfinder Satellite Observations) mission launched in 2006. CALIOP measures at two wavelengths 532 and 1064 nm, with the 532 nm detection being separated into orthogonal polarization components that are parallel and perpendicular to the polarization plane of the outgoing beam. The volume density of the particles can be determined by the amount of backscatter and the amount of depolarization of the scattered light is used to infer if the particle is spherical or not.

CALIOP is a nadir pointing lidar and so has the advantage over Solar Occultation measurements in that it provides a greater density of measurements as measurements can be made at any time as opposed to only at sunrise or sunset. Although in practice only nighttime measurements are used as higher background signals associated with scattering of solar radiation during the day make the signal to noise ratio too large to detect tenuous PSC [Pitts et al. 2007]. On average 300000 CALIOP measurements

are acquired per day at latitudes poleward of 55° [Pitts et al. 2007]. The difference in measurement density between CALIOP and solar occultation methods is important when considering spatially averaged PSC frequency. Figure 1.8 shows a comparison of CALIOP PSC frequency over the region 50°S - 82°S (top panel) with the same using only CALIOP measurements sub-sampled at locations observed by a solar occultation method (SAM II) (lower panel); the later produces significantly higher PSC frequency. During June SAM II samples only at lower latitudes (~65°S) and so underestimates the average PSC frequency and during September samples only near the pole (~80°S) and hence overestimates the average PSC frequency [WMO 2010].

Chapter 2

Literature Review: PSC Particle Types and Formation Mechanisms

2.1 PSC Types

PSC types are grouped by their optical properties, namely the amount of backscatter, from which the volume density of the PSC can be inferred; the colour ratio (ratio of backscatter at different wavelengths), from which size can be inferred and depolarization, from which the shape (how aspherical the particle is) can be inferred. Using lidar observations from Browell et al. [1990], Toon et al. [1990] designates the PSC categories 1a, 1b and 2. Type 1a is highly depolarizing (and therefore aspherical) and has low backscattering ratios, it is assumed to be NAT or nitric acid dihydrate (NAD) with an equivalent radius of 1 μm or larger. Type 1b, assumed to be STS, is not depolarizing and has low backscattering ratios; they are therefore spherical and typically have a radius of 0.5 μm. Type 2 has large backscattering ratios and high depolarization, based on this and the observation that these particles are found at temperatures below the water ice frost point [Poole and McCormick 1988] these particles are believed to be composed of ice.

2.2 Equilibrium Temperatures

The temperature threshold T_{NAT} originates from a laboratory study conducted by Hanson and Mauersberger [1988] on the vapour pressures over NAT crystals. The experiment consisted of forming a small amount of NAT crystal on a glass surface by vapour deposition and then adding or removing water vapour at constant temperature to reach equilibrium whereupon the HNO_3 and H_2O vapour pressures are measured. A similar study was conducted by Marti and Mauersberger [1993] on the vapour pressure over

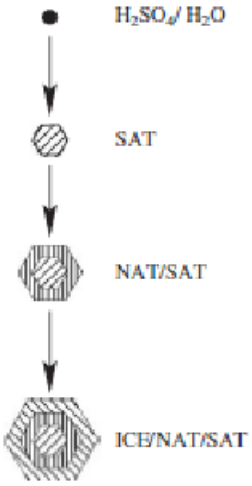

Figure 2.1: Three stage model of PSC formation (Source: Lowe and MacKenzie [2008])

ice at temperatures typical of the stratosphere which gives the water ice frost point threshold temperature T_{ice}. Hanson and Mauersberger [1988] find the NAT equilibrium function to be:

$$Log\left(P_{HNO_3}\right) = m\left(T\right) Log\left(P_{H_2O}\right) + b\left(T\right) \tag{2.1}$$

where P is in Torr and

$$m\left(T\right) = -2.7836 - 0.00088T,$$
$$b\left(T\right) = 38.9855 - 11397.0/T + 0.009179T$$

this equation being valid between 180 and 200K.

Marti and Mauersberger [1993] fit the following equation to the ice equilibrium data:

$$Log\left(P_{H_2O}\right) = \frac{-2663.5}{T} + 12.537 \tag{2.2}$$

this equation being valid between 170 and 253K.

At a height of 50kPa and with 5 ppmv H_2O and 10 ppbv HNO_3 (which are typical of the stratosphere) T_{NAT} is 195.7 K and T_{ice} is 188.4 K. Below these thresholds the solid particle is more thermodynamically favourable than the vapour phase.

However, despite this knowledge particular mechanisms of PSC formation are still a topic for debate. Figure 2.1 shows a schematic of the three stage model; one of the earlier models of PSC formation. A more complicated model from [Tabazadeh et al. 1994] is shown in Figure 2.2. Sections 2.3, 2.4, and 2.5 discuss the different PSC types and their possible formation mechanisms.

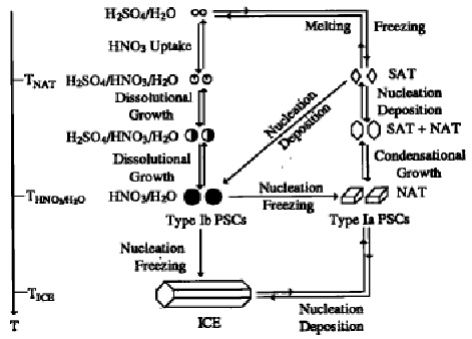

Figure 2.2: A more complex model of PSC formation (Source: Tabazadeh et al. [1994])

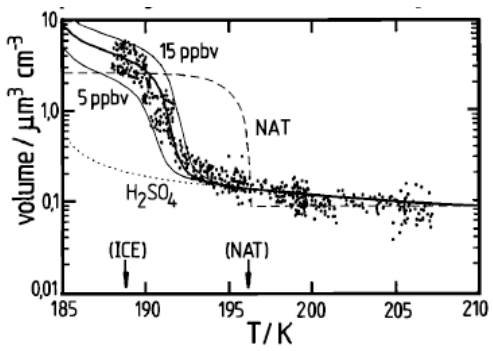

Figure 2.3: Growth of STS aerosols (Source: Carslaw et al. [1994])

2.3 Type 1b PSC

In the lower stratosphere there exists a layer of aerosols composed of sulphuric acid and water. The properties of these aerosols, namely the composition, size and optical properties, were investigated by Steele and Hamill [1981] who performed theoretical calculations of the properties for a range of temperatures and humidities typical of the stratosphere. At cold temperatures these H_2SO_4/H_2O aerosols absorb other gases such as HCl, HBr, HOCl, HOBr and particularly HNO_3 as well as further H_2O. Such aerosols composed of $H_2SO_4/HNO_3/H_2O$ are known as supercooled ternary solution (STS). Carslaw et al. [1994] modeled the particle growth and composition change due to the uptake of HCl, HNO_3 and H_2O by the aerosol as a function of temperature. It was found that the rapid aerosol growth occurred as the temperature was decreased below approximately 192 K (for a 55 hPa altitude and 5 ppmv H_2O, 10 ppbv HNO_3 and 1 ppbv HCl) due to uptake of HNO_3 as shown in Figures 2.3 and 2.4 taken from Carslaw et al. [1994]. The uptake of HNO_3 and H_2O is so significant that at temperatures of 190 K and below the concentration of H_2SO_4 in the aerosol decreases to below 2%. These results concur with other thermodynamical models of liquid droplets [Cox et al. 1994; Tabazadeh et al. 1994] which show rapid change in composition between H_2SO_4/H_2O and HNO_3/H_2O at about 4-5 K above the frost point.

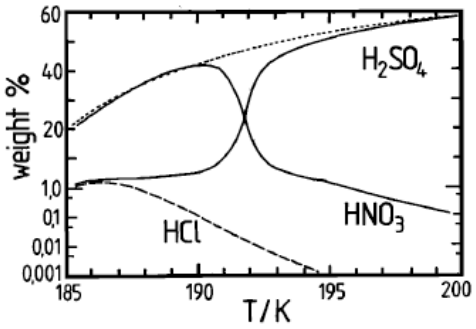

Figure 2.4: Composition change of STS aerosols (Source: Carslaw et al. [1994])

2.4 Type 2 PSC

In examining airborne lidar data obtained over the Arctic, Poole and McCormick [1988] noticed that particles observed below the frost point were larger than those above. These observations lead to the differentiation of Type 1 and Type 2 PSC [Turco et al. 1989], where Type 1 was considered to be μm sized nitric acid hydrate particles and Type 2 larger (10-100 μm) ice particles. Initially it was assumed by Poole and McCormick [1988] and also Hanson and Mauersberger [1988] that these ice particles form by vapour deposition on Type 1 particles however it soon became clear that observational evidence did not support this idea.

A more recent proposed formation mechanism is the vapour deposition of ice onto Sulphuric Acid Tetrahydrate (SAT) particles. Fortin et al. [2003] performed laboratory experiments to investigate this mechanism and found SAT to be an efficient nucleus for ice formation, only 0.1-1.3 K of supercooling below the frost point was required for nucleation to occur. Koop and Carslaw [1996] show that SAT is the thermodynamically stable form of H_2SO_4/H_2O between 188 and 213 K but 'deliquesces' at temperatures 2-3 K above the frost point in the presence of HNO_3 (although strictly speaking 'deliquescence' refers to solid to liquid phase change due to the uptake of water vapour). However, Iraci et al. [1998] in testing Koop and Carslaw's theory found that only 63% of SAT samples (in thin film form) exhibited some amount of deliquescence at the predicted temperature, which provides limitations to this formation mechanism.

Homogeneous freezing of ice out of aerosols (STS as well as binary H_2SO_4/H_2O or HNO_3/H_2O) is another proposed formation mechanism. Laboratory experiments such as Chang et al. [1999] (regarding STS and HNO_3/H_2O), Koop et al. [1998] and Middlebrook et al. [1993] (regarding H_2SO_4/H_2O), have shown this to be a valid mechanism with ice typically nucleating with around 2-3 K supercooling below the frost point. Theoretical studies such as MacKenzie et al. [1995, 1997, 1998] are consistent with these results. There is however some debate over whether the nucleation is surface or volume based. In developing a thermodynamic scheme for ice nucleation Koop et al. [2000] assumes nucleation to occur within the interior of the droplet while Tabazadeh et al. [2002] advocates the importance of the gas-liquid interface for nucleation.

2.5 Type 1a PSC

Type 1a PSCs are non-spherical particles around 1 μm in radius, as deduced from lidar observations by Toon et al. [1990]. These particles are believed to be composed of NAT as in-situ [Arnold et al. 1989; Fahey et al. 1989] and remote sensing [Santee et al. 1998; Toon et al. 1989] measurements of total reactive nitrogen or gaseous HNO_3 have demonstrated that PSCs contain nitrates. Additionally, Hanson and Mauersberger [1988] showed that the stable hydrate under stratospheric conditions is the trihydrate (NAT). Although experiments by Worsnop et al. [1993] show that other hydrates are metastable, in particular the dihydrate NAD is only slightly less stable than NAT and forms more readily. This is supported by theoretical studies by Natsheh et al. [2006], who also finds that the formation of NAT was more thermodynamically favourable from nitric acid and the monohydrate NAM than from NAD, although these processes are also kinetically limited under stratospheric conditions.

Höpfner et al. [2006] compared MIPAS spectral measurements of PSCs that were identified and classified by coincident lidar observations, with the refractive indices of expected PSC constituents. It was found that observations of type 1a PSC which has a prominent spectral band at 820 cm^{-1} matches the refractive properties of NAT, however NAD (which has a prominent spectral band at 810 cm^{-1}) was not observed. However, Kim et al. [2006] used transmittance data from the Improved Limb Atmospheric Spectrometer-II (ILAS-II) to deduce the composition of PSC and found that of the 83 cases studied, two could be described as a NAD/NAT mixture (compared to 28 that were purely NAT).

There exist a number of theories regarding the formation mechanism of NAT or NAD. One such mechanism is homogeneous freezing of STS droplets. In bulk freezing experiments Molina et al. [1993] found that STS would freeze to NAT at NAT supersaturation ratios of >10. Iraci et al. [1995] observed NAT crystallization on H_2SO_4 thin films for supersaturations of >14. Koop et al. [1995, 1997b] uses bulk freezing experiments to calculate a limit on the freezing rate for STS droplets. As nucleation is a stochastic process an upper bound on the freezing rate may be calculated from a single experiment, using Poisson statistics. For example a 1 ml sample that freezes at 1000s allows the upper bound freezing rate, Ω, to be calculated using the following equation:

$$\Omega = \frac{1}{\tau} \ln\left(\frac{1}{1-x}\right) \tag{2.3}$$

where τ is the time to freeze and x is the confidence level. Using a confidence level of 99% gives an upper bound freezing rate of 0.0046 s^{-1}, which for the 1 ml sample corresponds to a nucleation rate of 0.0046 $cm^{-3}s^{-1}$. Applying this nucleation rate to a droplet with a volume of 1×10^{-12} cm^3 gives a freezing rate of 4.6×10^{-15} s^{-1}. Koop et al. [1995] concluded that the nucleation rates are too small to be of importance in the stratosphere. Similar work by Knopf et al. [2002] concurs with this conclusion, finding nucleation rates of $<2\times10^{-5}$ $cm^{-3}s^{-1}$ and $<8\times10^{-2}$ $cm^{-3}s^{-1}$ for NAD and NAT

respectively. Koop et al. [1995] does however allow for an exception wherein aerosols with extremely low (<0.01 wt%) H_2SO_4 might possibly have a high enough nucleation rate to be significant. The above studies assume volume-based nucleation; however, as with the freezing of ice, Tabazadeh et al. [2002] proposes that the process is in fact surface-based which ought to allow for higher nucleation rates. Most of the evidence points toward homogeneous nucleation not being significant in the stratosphere, although there is no consensus on the matter.

Another possible mechanism is heterogeneous nucleation by vapour deposition on a solid particle, such as ice or SAT. Wofsy et al. [1990] produces a model of NAT nucleation and growth by heterogeneous nucleation, finding particle formation to occur for supercooling of 1-4 K. In an effort to explain the existence of ice particles observed at temperatures 5-10 K above the frost point, Peter et al. [1994] theorizes a mechanism wherein during rapid cooling NAT condenses along with ice on ice particles; as this particle warms the outer ice would preferentially evaporate leaving an ice particle with NAT coating that prevents further evaporation. This theory was tested by Middlebrooks et al. [1996] who found that the presence of small amounts of NAT in ice did inhibit evaporation, specifically samples with 80:1 and 150:1 H_2O:HNO_3 compositions evaporated at temperatures of 8 and 3 K higher than pure ice, respectively. Although, Biermann et al. [1998], performing similar experiments found there to be no significant slowing of the evaporation. Middlebrooks et al. [1996] performed the experiment in a vacuum whereas Biermann et al. [1998] used a vessel containing H_2O and HNO_3 with controlled mixing ratios which may account for the differing results.

SAT is another candidate nucleus for vapour deposition of NAT. However, theoretical studies by MacKenzie et al. [1995] have shown that this process is unlikely to occur. Iraci et al. [1995] found experimentally that a supersaturation ratio of >130 is required for NAT to form on SAT. Zhang et al. [1996] similarly finds that large (>60) supersaturations are required for NAT formation, although they note that SAT particles that had been previously coated with NAT exhibited greater nucleation efficiency.

2.6 CALIOP PSC classes

Most of the observational data divides the PSC into the three types described in the previous sections, however the composition of PSC is divided differently in the CALIOP data used in this research. Citing that PSC are often observed as mixtures of the different types, Pitts et al. [2009] proposes classes that take this into account. Further analysis of CALIOP data by Pitts et al. [2011] extends the number of classes, splitting PSC into the following classes:

- STS
- Mix 1, which is STS with a small amount of NAT
- Mix 2, STS with a larger amount of NAT

- Mix 2 enhanced, as for Mix 2 but with stronger backscatter provided by larger NAT particles with greater number density
- Ice
- Wave Ice, larger ice particles believed to have been formed by gravity wave temperature fluctuations

The class divisions are based upon the polarization ratio δ_{532} (ratio of perpendicular and parallel backscatter components) the backscatter ratio of the 532 nm signal R_{532} (ratio of the total backscatter and the molecular backscatter). Further discussion of the CALIOP instrument and data can be found in section 3.3.

2.7 Gravity Waves

Gravity waves are perturbations caused by a vertical disturbance of a horizontal fluid flow; they are often caused in the atmosphere by air moving over mountains (and in this case are known as mountain waves or orographic waves). The wave-like perturbations are due to the competing gravitational and buoyancy (as the density of the atmosphere decreases with altitude) forces acting to oscillate a vertically displaced air parcel. Mountain waves can produce large temperature fluctuations, using balloon measurements Hertzog et al. [2007] measured a 17 K fluctuation at around a 17 km altitude over the Antarctic Peninsula. It is thought that temperature fluctuations in gravity waves are important in the formation of PSCs.

Numerous studies identify instances where PSC formation can be explained by gravity waves decreasing mesoscale temperatures in regions where the synoptic scale temperature would otherwise be too warm for PSC formation. For example McDonald et al. [2009] uses POAM III aerosol extinction measurements to identify areas of PSC and compares these with temperature measurements. They find when temperatures are close to the threshold T_{NAT} during June (the start of the PSC season) 40% of observed PSCs may be attributed to gravity wave temperature fluctuations, this decreases to 15% during the rest of the PSC season where synoptic temperatures below T_{NAT} are more common. Alexander et al. [2011] concludes that gravity waves caused by the mountainous Antarctic peninsula account for 30% of the total PSC spatial volume, and in particular 50% of the spatial volume of ice PSC, in the 60-70°S latitude band during the winter of 2007. Eckermann et al. [2009] finds that a particular sudden outbreak of NAT particles observed around the edge of the Antarctic polar vortex in June 2003 can be attributed to gravity waves over the Antarctic Peninsula. It is proposed that the gravity waves form ice particles which nucleate the NAT particles. The progression of the outbreak is shown in Figure 2.5 where the red squares represent NAT with radii <3 μm, green circles represent either STS or larger NAT or tenuous ice, and blue triangles are ice, the orange region is where the temperature is below T_{NAT} and above T_{STS}. Gravity waves were detected over the period 10-15 June using AIRS (Atmospheric Infrared Sounder)

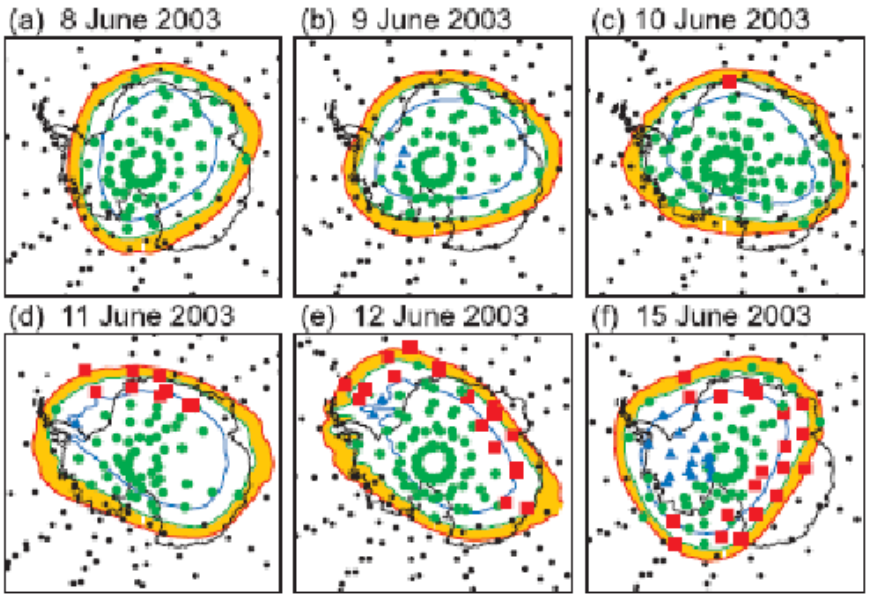

Figure 2.5: An outbreak of NAT observations downstream of the Antarctic Peninsula (Source: Eckermann et al. [2009])

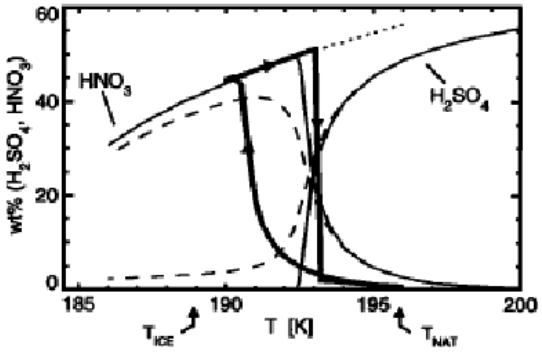

Figure 2.6: Non-equilibrium composition change of an STS aerosol (Source: Meilinger et al. [1995])

data, and NAT particles can be seen propagating downstream of the Antarctic Peninsula over this period. In the Arctic, Svendsen et al. [2005] uses a microphysical model to simulate NAT formation with and without mountain waves and finds that mountain waves account for a 10% increase in NAT production.

As well as aiding PSC production by decreasing the local temperature from synoptic levels it has been suggested that rapid cooling rates caused by gravity wave may be important for PSC formation. Meilinger et al. [1995] model the composition change of STS under non-equilibrium conditions caused by rapid temperature fluctuations. Figure 2.6 shows the composition of a droplet that is cooled from 196 K to 190 K over an hour, held constant for an hour then raised back to 196 K over an hour. Under infinitely slow cooling the concentrations follow the dashed lines with HNO_3 peaking at 41 wt%, the bold lines show the non-equilibrium temperature fluctuation where the droplet became

binary HNO_3/H_2O and reached a peak HNO_3 concentration of 51 wt%. This temperature fluctuation represents a relatively mild gravity wave, using temperatures from a realistic gravity wave trajectory with a cooling rate of 36 Kh^{-1} peak HNO_3 increased to 52.1%. Aerosols with such large HNO_3 and extremely small H_2SO_4 concentrations are potentially able to freeze according to Koop et al. [1997b]. Using larger temperature fluctuations (150 Kh^{-1}) Tsias et al. [1997] modeled that aerosols with 58% HNO_3 could be produced. They were also able to show experimentally that such aerosols would freeze to NAD. Rather than freezing out of STS, Luo et al. [2003] suggests that high NAT supersaturations instead lead to NAT formation by vapour deposition on ice particles, although they note that this mechanism produces PSCs with higher number density ($>10^{-2}$ cm^{-3}) for typical cooling rates and is unlikely to directly cause lower number density PSCs.

Chapter 3

Data and Trajectory Model

3.1 MERRA

The temperature and wind data used in this study comes from the MERRA (Modern Era Retrospective-analysis for Research and Applications) high resolution reanalysis provided by the NASA GMAO (Global Modeling and Assimilation Office) which is based on the GEOS-5 DAS (Goddard Earth Observing System Data Assimilation System Version 5) assimilation system. In each 6-hourly dataset the GEOS-5 system assimilates approximately two million observations of standard atmospheric variables such as temperature, pressure and wind components from sources including weather stations, balloons, aircraft, ships, buoys, and satellites [Rienecker et al. 2011]. The GEOS-5 assimilation uses a 1/2° latitude and 2/3° longitude horizontal grid and 72 pressure levels from the surface to 0.01 hPa. The data used for this study is from the DAS 3d analyzed state on pressure (inst6_3d_ana_Np) product. This uses the native horizontal grid, but with a reduced vertical resolution of 42 levels from 1000 to 0.1 hPa. For each day, four data points are given at each grid point, corresponding to the instantaneous value of the respective variable in six hour increments.

3.2 MLS

The data for the H_2O and HNO_3 mixing ratios is obtained from the Earth Observing System (EOS) Aura Microwave Limb Sounder (MLS) version 3.3. The instrument measures the radiance in the millimetre and sub-millimetre range along the atmospheric limb [Waters et al. 2004]. In addition to H_2O and HNO_3 this instrument measures 13 other gaseous species as well as temperature and geopotential height (this temperature data was not used as its horizontal and vertical resolution is more coarse than that of the MERRA dataset). The instrument contains five radiometers measuring different spectral regions, H_2O and HNO_3 is primarily identified by the 190 GHz radiometer. The Aura satellite has an orbital inclination of 98° meaning measurements can be made between

latitudes of 82°N and 82°S. The field of view at the tangent point of the limb of this radiometer is 4.5 km in the vertical and 9 km in the horizontal direction. 240 limb scans are performed per orbit which means a measurement approximately is made every 24.7 s (corresponding to a 165 km along track resolution). The vertical coordinate is pressure, HNO_3 has measurements at 36 levels between 1000 and 0.000001 hPa with 6 per decade between 1000 and 0.1 hPa and 3 per decade at higher levels, H_2O has 52 measurements over the same range with 12 per decade between 1000 and 1 hPa, 6 between 1 and 0.1 hPa and 3 per decade at higher levels. The range in which measurements are considered acceptable for scientific use, however are 100-0.46hPa for HNO_3 and 316-0.0002hPa for H_2O. The dataset was quality controlled according to the guidelines in Livesey et al. [2011]. Information on the validation of the HNO_3 MLS product can be found in Santee et al. [2007] and the H_2O product in Read et al. [2007] and Lambert et al. [2007].

3.3 CALIOP

PSC data is obtained from the CALIOP (Cloud Aerosol Lidar with Orthogonal Polarization) instrument from the CALIPSO (Could Aerosol Lidar and Infrared Pathfinder Satellite Observations) mission launched in 2006. The CALIPSO satellite orbits on the same path as the Aura satellite, so is able to observed PSC as far south as 82°. The lidar has a pulse rate of 20.25 Hz which allows a profile measurement every 333 m along the satellite path. In the area of interest, poleward of 55°S, 30000 lidar profiles are measured per day. The fundamental vertical resolution of the instrument is 30 m, although on-board averaging of the data decreases the resolution to 180 m in the vertical and 1.67 km in the horizontal direction in the lower stratosphere. Only nighttime data is used due to the increased background noise level during daytime.

The lidar uses two frequencies 532 and 1064 nm and measures the parallel and perpendicular component of the 532 backscatter separately. PSCs are detected in the backscatter data as statistical outliers above the returns linked to background atmospheric aerosols. In order to detect thin cloud the backscatter data is averaged over increasingly coarse horizontal distances of 5, 15, 45, and 135 km, each time removing data that has been identified as cloud at finer resolutions and recalculating the threshold level. False positives are minimized by using a spatial coherence test over the 15 points surrounding the point in question. In the original detection algorithm Pitts et al. [2007] used only the backscatter ratio at 532nm to identify PSC. The backscatter ratio R_{532} is the ratio of total backscatter at 532 nm β_{532} to the molecular backscatter β_m at this wavelength; this is a measure of the volume density of the PSC.

$$R_{532} = \frac{\beta_{532}}{\beta_m} \tag{3.1}$$

In version 2 of the algorithm [Pitts et al. 2009] depolarization ratio measurements were added to improve PSC identification. The polarization ratio $\delta_{aerosol}$ is the ratio of

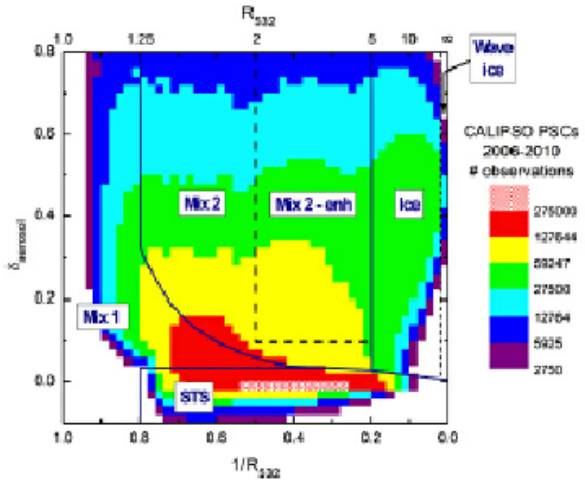

Figure 3.1: Classification of the CALIOP data (Source: Pitts et al. [2011])

the perpendicular to the parallel component of the backscatter, this is an indicator of the shape of the particle with spherical particles having low polarization ratios and higher ratios indicating that the particle is more aspherical. The PSC categories in this algorithm are STS, Mix 1, Mix 2 (mixtures of STS and NAT, with Mix 2 having higher concentrations of NAT than Mix 1) and ice. The R_{532} and $\delta_{aerosol}$ thresholds for these categories are shown in Figure 3.1 with solid lines. The categories were extended by Pitts et al. [2011] to include Mix 2 enhanced (Mix2enh) and wave ice, thresholds for these categories are shown by dashed lines in Figure 3.1. The Mix2enh category represents a population of observations where the backscatter signal is consistent with NAT particles that have a sufficiently high number density and volume such that they are not masked by STS aerosols. Wave ice is ice PSC with very high number density believed to have been formed by rapid temperature fluctuations linked to gravity waves. The wave ice category was identified by examining the colour ratio of the backscatter, which is the ratio between the backscatter at 1064 and 532 nm. The colour ratio gives a measure of the particle size using Mie scattering theory. Although colour ratio is not explicitly a part of the detection algorithm it was noticed that there existed a population of the observations that had high backscatter ratios with anomalously low colour ratios so observations from the ice category with large backscatter ratios were assigned to the separate wave ice category. Although the category is named wave ice this does not necessarily preclude particles categorized as ice from having formed in gravity waves.

3.4 Trajectory Model

In order to investigate conditions required for the formation of PSC the temperature history along the back trajectory of PSC observations is examined. A simple two dimensional Lagrangian trajectory model is used to find this temperature history. The model is effectively two dimensional as the air parcel can be assumed to move along a

surface of constant potential temperature; the assumption being that the motion of the air parcel involves only adiabatic processes. Potential temperature, θ, is the temperature an air parcel at a pressure of P would have if it were lowered adiabatically to a reference pressure level P_0 (usually 1000 mbar). It may be calculated with Poisson's equation:

$$\theta = T\,(P_0/P)^{(R/c_P)} \tag{3.2}$$

where T is the temperature of the air parcel at pressure P, R is the universal gas constant and c_P is the specific heat capacity at constant pressure. The surface of constant potential temperature can also be called an isentropic level as reversible adiabatic processes are isentropic.

MERRA winds and temperatures that have been interpolated from pressure levels onto isentropic surfaces are input into the model. The trajectory, beginning from a prescribed point, is then calculated at hourly intervals using a fourth order Runge-Kutta method with winds that have been linearly interpolated in time and bilinearly interpolated in space. The MERRA winds are given in zonal and meridional components so in order to avoid problems associated with the singularity at the pole [Garney et al. 2007] calculations for latitudes poleward of 70°S are transformed in to Cartesian coordinates. At each point along the trajectory the temperature is similarly interpolated and the H_2O and HNO_3 mixing ratios are recorded. The H_2O and HNO_3 concentrations are used to calculate the equilibrium temperatures T_{NAT} and T_{ice} by solving equations 2.1 and 2.2 from section 2.2.

Some idea of the accuracy of trajectory model can be gained from Rolph and Draxler [1990]. Using a second order solution method they found that the absolute horizontal transport deviation (AHTD) for a four day trajectory calculated from winds with 6 hr and 90 km resolution was 411 km. The spatial resolution of MERRA data is 0.5° latitude by 0.667° longitude which works out to be 55 by 37 km at 60° latitude, and the solution method is of higher order so a lower AHTD should be expected. Other sources of error include turbulence and violations of the isentropic assumption.

As the MLS mixing ratio data is only provided at a resolution of 165 km along the satellite path, spatial and temporal averages are used as input into the trajectory model. Initially a method of finding points where the trajectory and the MLS satellite were coincident (defining 'coincident' as within 300 km) and using mixing ratio data from these points to interpolate along the rest of the trajectory was used. However it was decided that this method was too computationally expensive considering over seven million trajectories were to be calculated. In addition, the coincident points were too sparse, on average only about four coincident points were obtained along a four day trajectory, in part this is due to the sparseness of the MLS data and also that the direction of rotation of the polar vortex and the satellite path were such that it was usually the case that the trajectory and the satellite are moving in opposite directions. Instead MLS observations were averaged in bins with dimension 5° latitude, 30° longitude and 7 days; this bin size

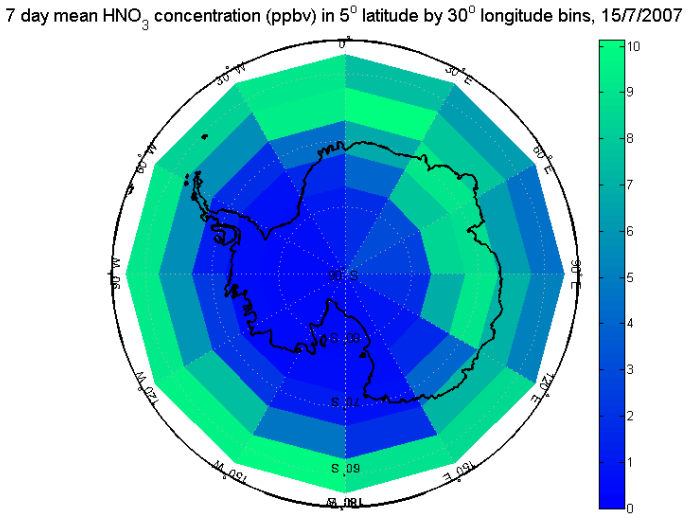

Figure 3.2: An example of the HNO_3 distribution averaged over 7 days into 5° latitude by 30° longitude bins for the 1st of July 2007

was chosen to ensure that a suitably large (>50) sample of MLS measurement would be contained in each bin. The temporal aspect of the bin is a moving average such that a bin average is the average over the previous three, current, and next three calendar days. These bin averages were then used to assign mixing ratio data to each point along a trajectory. An example of the bin averages for the HNO_3 concentrations are shown in Figure 3.2.

A CALIOP observation is assigned to each trajectory, instead of just assigning the closest measurement to the isentropic level of the trajectory a more complex algorithm is used which accounts for possible sedimentation of a PSC particle. Sedimentation is an issue as particles formed in an air parcel moving along an isentropic trajectory may not be observed on that isentropic level at the end of the trajectory as they may have fallen some distance due to gravity. Figure 3.3 shows the terminal velocity of PSC particles as a function of particle radius. For STS aerosols which are typically ~0.5 μm sedimentation will be negligible, NAT particles that are 1-2 μm will have a sedimentation velocity of around 100 m/day, while ice may have a large range of sizes and could have sedimentation velocities of 1 km/day or more.

The height corresponding to the isentropic level of the trajectory is found by first calculating the pressure using equation 3.2 and then converting this to height using NASA's Earth Atmosphere Model [NASA 2010], the equation applicable in the lower stratosphere being:

$$P = 22.65 \exp\left(1.73 - 0.000157h\right) \tag{3.3}$$

Five CALIOP measurements are then identified based on this height, the one immediately above this height and the four immediately below. The algorithm the looks for

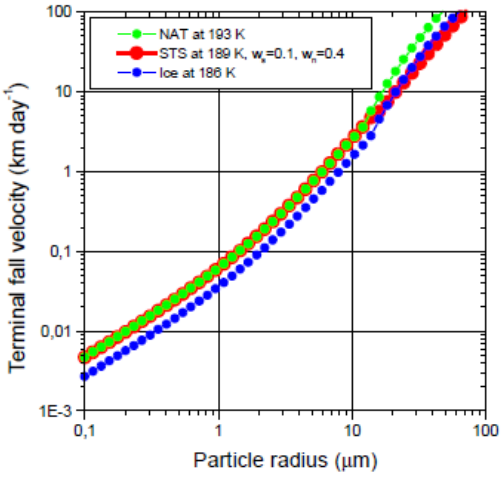

Figure 3.3: Terminal velocity of PSC particles as a function of particle radius (Source: Larsen [2000])

PSC types in regions that they be expected based on their estimated fall velocity, namely STS in the top two, NAT types in the top three and ice in the lower four. The first level of the algorithm looks at all five points, if four or more are clear of PSC then the trajectory is identified as clear or if three or more are PSC of one class then the trajectory is associated with that class. The next level looks for two points of the same class within the expected region of the given class. If the trajectory remains unassociated the next level looks for one point within the expected region, looking first for wave ice then ice, Mix2enh, Mix2, Mix1 and lastly STS. The order of this hierarchy was decided upon by putting the particle classes with the highest backscatter ratio (see Figure 3.1) at the top, with the assumption that they were the most likely to be correctly identified in the CALIOP algorithm; STS was placed lowest as it was deemed most likely to be misidentified based on Pitts et al. [2012] finding that approximately 6% of STS is misclassified NAT mixtures. After this level all remaining trajectories are identified as clear.

The nature of this algorithm does skew the proportion of observations slightly. Comparing the set of observations associated with the trajectories with the sum of all observations over 20 height levels (selected to cover variations in the 450 K isentropic level) shows that clear and STS observations are under-represented in the trajectory observations set by 3.1 and 4.7%, respectively with all other classes being over-represented. This skewness however will be deemed acceptable in light of the previously mentioned finding of Pitts et al. [2012] and the potential for tenuous PSC to be identified as clear in the CALIOP observations.

Primarily this study uses trajectories calculated along the 450 K isentropic level as this corresponds closely to the centre of the height at which PSCs are found. At this level over seven million four day trajectories were calculated using the location of CALIOP measurements as starting points. These CALIOP measurements were from the 2007-2010 PSC seasons (June-September) over the polar region (south of 55°S). An example

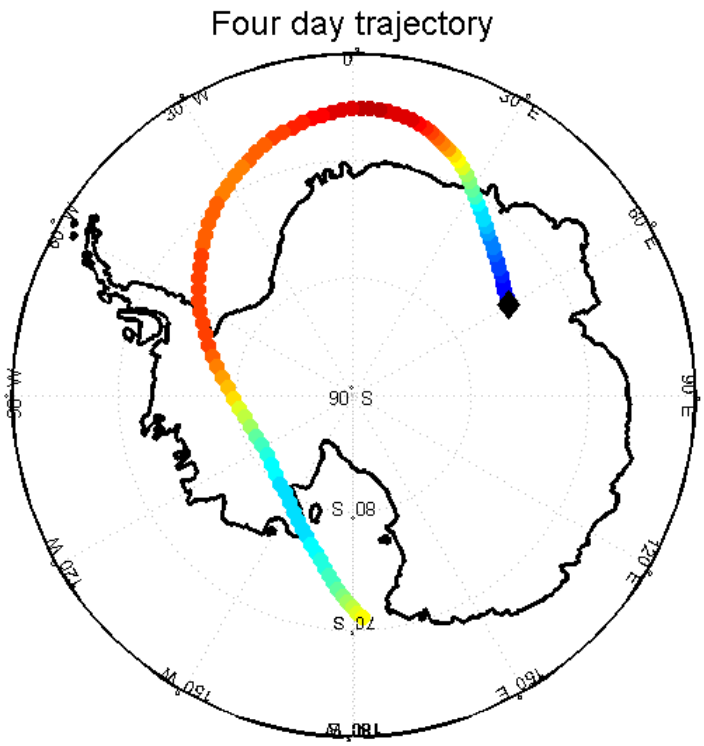

Figure 3.4: An example four day trajectory

four day trajectory and its associated temperature history is shown in Figures 3.4 and 3.5.

3.5 Microphysical Model of PSC Formation

PSC formation will also be investigated by running a microphysical model on temperature histories. The microphysical model used was developed by Niels Larsen and runs on temperature histories were preformed by Andrew Klekocuik. Figure 3.6 shows a schematic of the processes included in the model. Type 1b aerosols form by the dissolution or melting of SAT, type 2 particles form either by the freezing of type 1b aerosols by ice nucleation on NAT. In the freezing of type 1b aerosols scenario the HNO_3 forms a kernel of NAT within the larger ice particle. Type 1a particles can then subsequently form by the evaporation of this ice. It is also possible for type 1a particles to form by the nucleation of NAT on preactivated SAT (following the results of Zhang et al. [1996] showing NAT is more likely to nucleate on SAT that has previously been in contact with NAT). The model can either be run in "Eulerian" or "Lagrangian" modes, in this case these terms refer to radius space rather than the usual *space* space. In the Lagrangian mode the model begins with a range of particle sizes, each one representing a fixed number of particles per kg of air, at each iteration of the model the new size of each representative particle is calculated. In the Eulerian mode of the model the particles

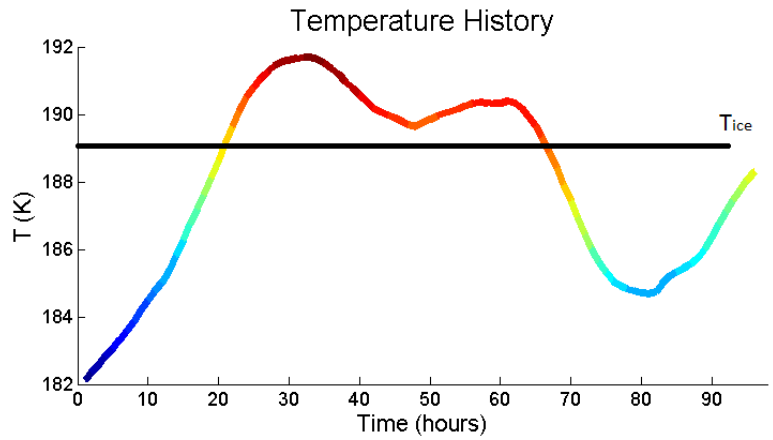

Figure 3.5: Temperature history corresponding to the trajectory in Figure 3.4

are divided into bins according to size and at each iteration particles are moved between bins according to particle growth or evaporation. In the Eulerian mode the model can operate across multiple atmospheric layers making it possible to model sedimentation with particles from bins corresponding to suitably large particle sizes dropping down to lower layers. Further description of the model can be found in Larsen [2000].

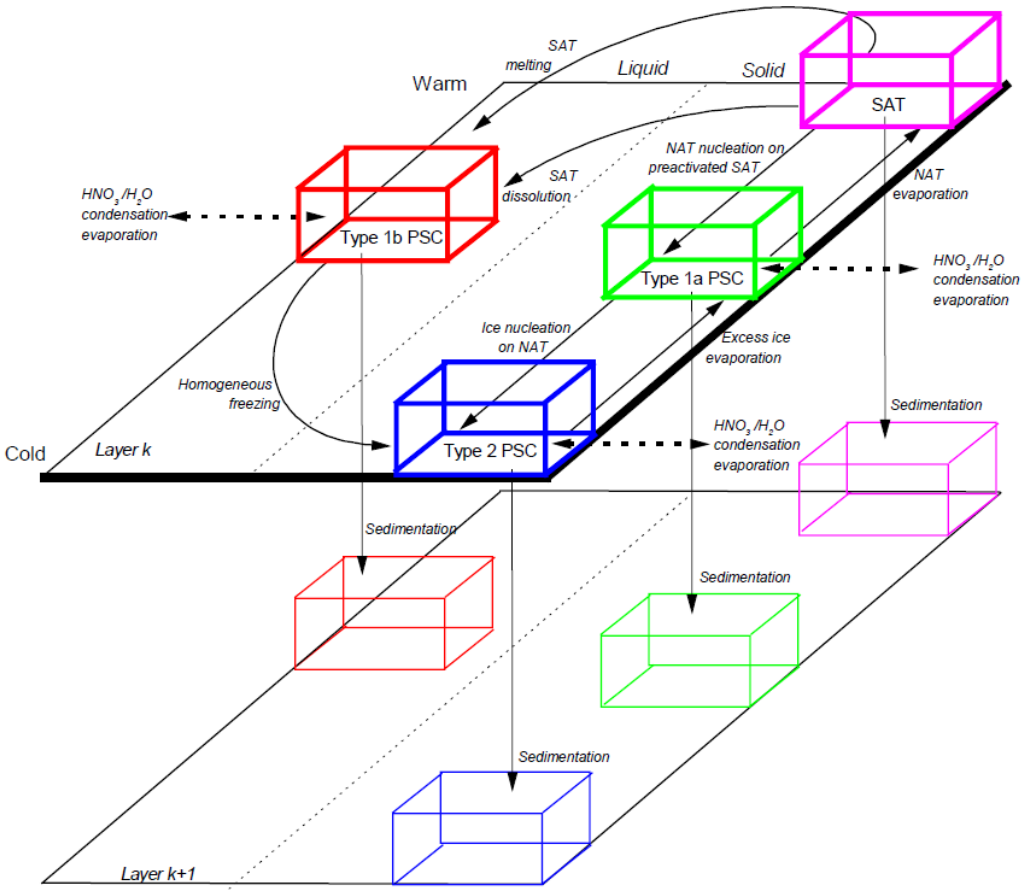

Figure 3.6: Schematic of the microhysical model of PSC formation (Source: Larsen [2000])

Chapter 4

Results and Discussion

This chapter presents the results of the analysis of the CALIOP PSC data with the aid of temperature histories derived by calculating the four day back trajectory using a Lagrangian model with wind velocities obtained form the MERRA reanalysis. As described in section 3.4, a trajectory was calculated beginning at the location of each CALIOP data point on the 450 K isentropic level. The 450 K level was chosen as it is close to the height where PSC is most abundant. The CALIOP data from the June-September period 2007-10 inclusive and south of 55°S which constitutes over seven million trajectories is examined. We will discuss how the results relate to different theories of PSC formation. Finally an algorithm for predicting the occurrence of different PSC types will be presented and the effectiveness of this system will be compared to the method of using simple temperature thresholds.

4.1 Occurrence of PSC

Initially the CALIOP observations will be shown simply in terms of the temperature at the time of observation. Figure 4.1 shows the frequency of observation of each PSC type[1] as a function of temperature. In cases where the T_{NAT} threshold is simplified further a value of 195 K is often used, 99% of the PSC occur below this threshold, but it is a few degrees below this temperature where the large increase in PSC occurrence happens - initially with STS which reaches peak a occurrence around 189 K. The occurrence of mixed classes increases slowly with decreasing temperature below 195 K, but do not reach their peak occurrence until temperatures of around 183 K. Ice has a peak occurrence at a similar temperature, but does not begin to occur until temperatures are below 189 K. On the 450 K isentopic level the mean pressure over the region and time period examined is 52 hPa, using 4.5 ppmv H_2O and 7 ppbv HNO_3 (which are typical of regions that have not be dehydrated or denitrified) gives a T_{NAT} of 195 K. This value however is shown to be too high to be a good threshold, a better threshold would be 192 K. More insight can

[1]For this and other figures the wave ice category will be omitted as it constitutes less than 0.05% of the observations at 450 K

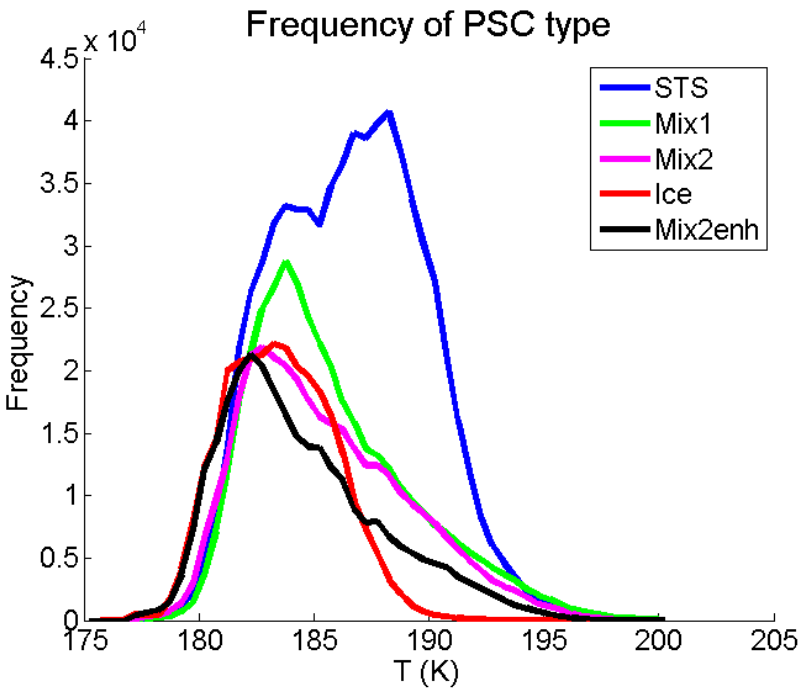

Figure 4.1: Temperature at which PSC classes are observed

be gained by plotting the frequency of occurrence relative to the applicable equilibrium temperature; T_{NAT} in the case of Mix1, Mix2 and Mix2enh, T_{ice} for ice and T_{STS} for STS; as shown in Figure 4.2. For the purposes of this figure and for the rest of the thesis T_{STS} will be defined as T_{NAT} - 4 K as this is approximately the temperature at which a rapid increase in aerosol size occurs [Carslaw et al. 1994]. Data are binned into 0.5 K bins.

In comparison to Figure 4.1 the distributions in Figure 4.2 are narrower. In particular the prominent high temperature tail in the distributions of the mixed classes in Figure 4.1 are reduced in Figure 4.2 where the distributions are much more Gaussian, this implies that the higher temperature NAT exists in regions of more abundant nitric acid. In Figure 4.1 the STS appears to be bi-modal, but is a single Gaussian in Figure 4.2, this is evidence of the occurrence being split between regions with different levels of denitrification. The shape of the distribution of ice changes less between the two figures, as water vapour is much more abundant than nitric acid in the stratosphere this means that dehydration has less impact.

For ice and STS the frequency distributions peak slightly below the equilibrium temperature and have a significant portion (31% and 36%, respectively) of the distribution above the threshold. In the case of STS this occurs because the formation temperature is not distinct, Figure 2.3 shows the rapid growth in STS particle size happens over a range of approximately 2 K. The occurrence of ice above the frost point is possibly explained by gravity waves; Pitts et al. [2012] provides evidence for this by examining January 2010 CALIOP data from the Arctic and finds that the anomalously warm ice observations occurred during the period in which gravity wave forcing was the primary

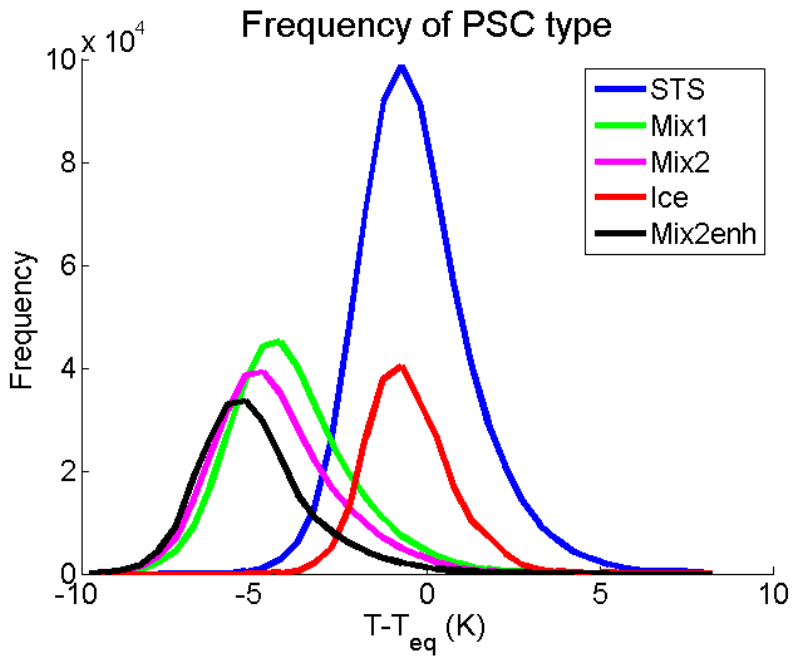

Figure 4.2: Frequency of observation by temperature relative to equilibrium

forcing for ice PSC formation. On the other hand the majority of the Mix categories are observed at temperatures 4 - 6 K below the equilibrium temperature (T_{NAT}). Also, the peak of the distribution occurs at lower temperatures for the mixed classes with higher NAT number density. Only a small fraction of NAT is observed at temperatures above the equilibrium temperature. This hints that T_{NAT} is not an effective threshold for NAT PSC occurrence.

The non-suitability of T_{NAT} as a threshold is better illustrated in Figure 4.3. This figure shows the probability of an observation with a given temperature (relative to T_{NAT}) showing a PSC of a certain type; the cyan line shows the total PSC observation probability. At temperatures near T_{NAT} there is only around 10% probability of observing any PSC and the probability only increases slowly as the temperature falls, indeed the temperature must be at least 5 K below T_{NAT} in order to obtain a better than 50% likelihood of a PSC observation. The probability of ice observations starts to increase rapidly around 6 K below T_{NAT}, generally the frost point is around 7 K below T_{NAT}. The other types, especially Mix 1 and Mix 2, show little effect of temperature on the probability of observation.

4.2 Is Temperature History a Factor?

The difference between the temperature histories of NAT and ice trajectories is illustrated in Figures 4.4 and 4.5. The figures show the distribution of the temperature relative to the respective equilibrium temperature at five hour increments along the back trajectories of particles of that type (Mix1, Mix2, and Mix2enh combined in the case of NAT). Note that equilibrium temperature varies along the back trajectory as

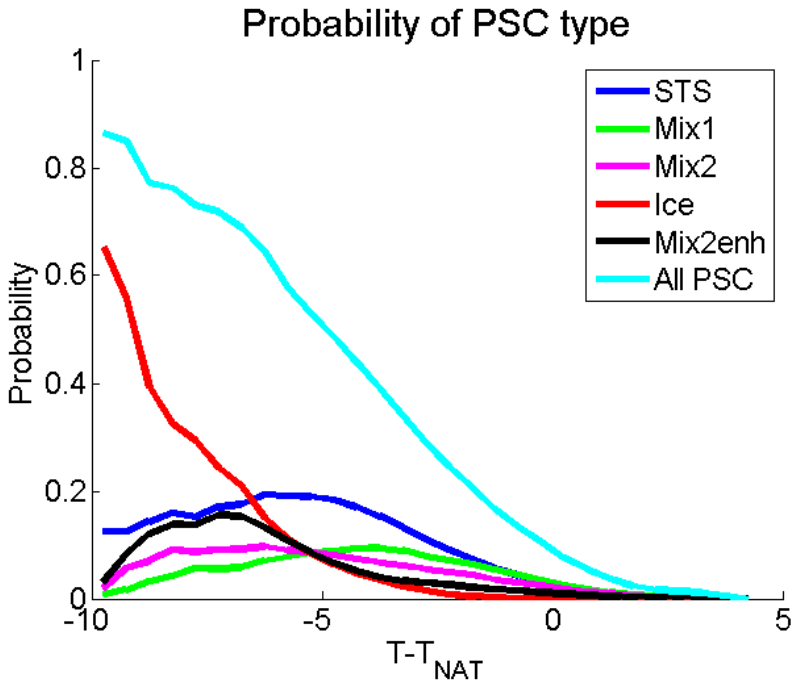

Figure 4.3: Probability of observation as a function of temperature relative to T_{NAT}

the H_2O and HNO_3 mixing ratios vary (see section 3.4). Comparison of the Figures 4.4 and 4.5 shows that the temperature distribution of NAT changes very little as time regresses. At t = 0, 2% of the distribution is above T_{NAT} and at t = 25 hours only 5% this distribution is above T_{NAT}. On the other hand, the temperature distribution of ice changes from a narrow distribution centred slightly below the frost point at the time of observation into a wide distribution that is close to that of the climatological temperature distribution within the space of about a day. At t = 0, 31% of the distribution is above T_{ice} and at t = 25 hours 73% this distribution is above T_{ice}. The rate of change of the temperature distribution of ice trajectories as seen in Figure 4.5 may only be indicative of how long an air parcel takes to cool to the requisite temperature for ice formation and that ice formation occurs relatively quickly, however the fact that the temperature profiles for NAT trajectories have a cold bias that persists for so much longer the those of ice suggests that the temperature history is a factor in formation of NAT.

The observation that NAT particles exist in air parcels that have been cold for a long time concurs with the work of Larsen et al. [1997] in which he examines 20 day back trajectories stemming from observations of PSC made by 30 balloon flights in the Arctic. It was found that temperature histories associated with type 1a PSC had last crossed below T_{NAT} a least one day previous to observation, and averaged a total of 102 hours below T_{NAT} between the time of observation and the time when temperature had been above the SAT melting temperature (~215 K). Instead of comparing this to ice observations Larsen et al. [1997] instead compares to type 1b observations which he finds typically cross below T_{NAT} less than 24 hours prior to observation and have spent on average 44 total hours below T_{NAT} since SAT melting occurred.

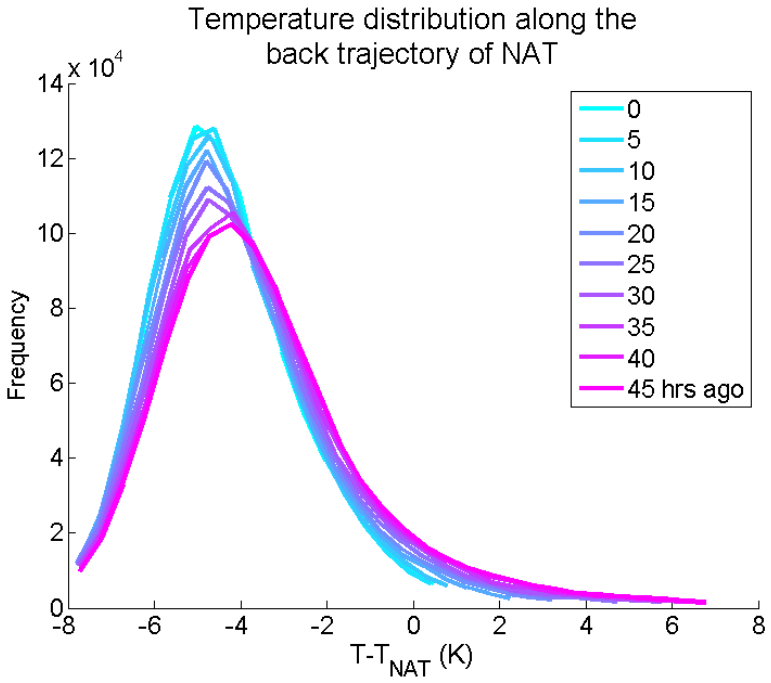

Figure 4.4: Temperature distribution at 5 hourly intervals along the back trajectories of NAT classes

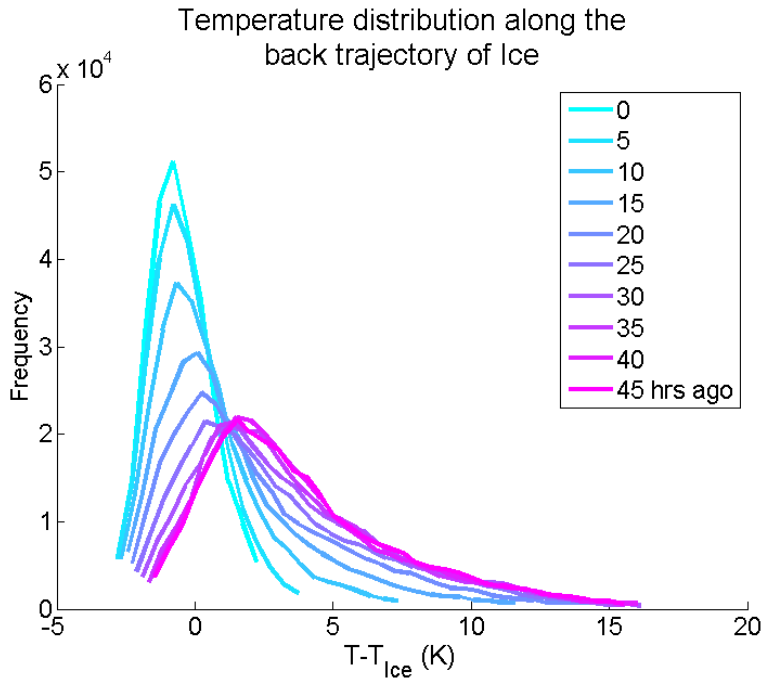

Figure 4.5: As for Figure 4.4 with ice particle trajectories

The information in Figures 4.4 and 4.5 is displayed in a alternate way in Figure 4.6. This figure shows the mean temperature histories, relative to the respective equilibrium temperature, of each PSC type and the range of temperatures indicated by the standard deviation (shaded region) and the 5^{th} and 95^{th} percentiles (dashed curves). Inspection of Figure 4.6 indicates that the mean temperature history of a NAT observation is only around one degree colder than it was 96 hours previous, whereas the mean trajectory for ice decreases around 4 K over the space of only 24 hours with an associated decrease in the standard deviation of the distribution. The mean NAT temperature is relatively constant over the four days and shows a smaller decrease in the standard deviation approaching the time of observation. Figure 4.6 shows that the NAT temperatures at t = 0 are significantly colder than the temperature threshold, with 95% of all NAT observations over one degree colder than T_{NAT}. At the time of the CALIOP observation (t=0) a significant portion of ice PSC have temperatures warmer than the temperature threshold (31%) and within 24 hours into the back trajectory the majority of ice observations are above the threshold. The STS temperature history characteristics fall in between those of ice and NAT. As was the case with ice there is a significant narrowing of the temperature range for times close to the the time of observation, however the decrease in mean temperature over the previous day is only around 1 K.

Figure 4.7 shows the mean trajectories of Mix1, Mix2, and Mix2enh which were combined to give the NAT mean trajectory in Figure 4.6. The mean temperature history of the Mix1 class stays relatively constant at 4 K below T_{NAT} over the entire four day period, while Mix2 and Mix2enh show decreases in the temperature of about 1 and 1.5 K over the 2 days prior to the observation, respectively.

In the case of ice the large change in mean temperature and the decrease in standard deviation prior to observation suggest that the temperature at the time of observation is of primary importance with perhaps some influence of the cooling rate. The implication being that ice forms relatively quickly. For Mix1, on the other hand, the mean temperature history is relatively constant and there is minimal decrease in the standard deviation indicating that the temperature history as a whole is important in determining the formation of Mix1. The implications of this result for the possible formation mechanisms of NAT is not entirely clear. It may highlight that persistent low temperatures are required to form NAT by the freezing of STS [Iraci et al. 1995; Molina et al. 1993] with low nucleation rates. Low amounts of NAT is the characteristic of the Mix1 class so this fits with this theory. However, the mean temperature is only 4 K below T_{NAT} which is the estimate of T_{STS} being used meaning that on average STS will not be present for the entire time in these trajectories. The Mix 2 and Mix2enh classes fall in between these two examples.

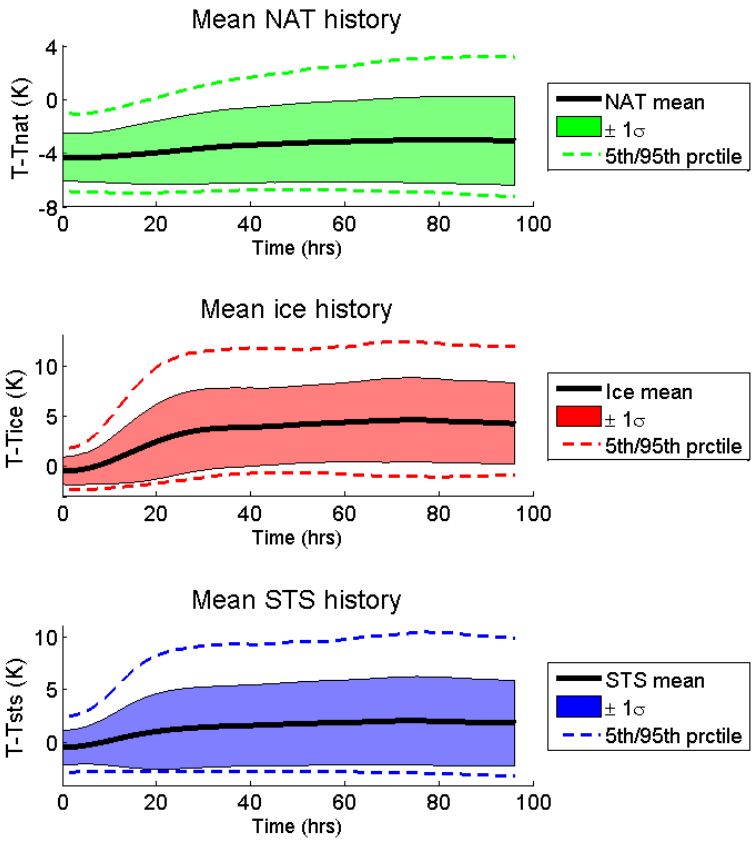

Figure 4.6: Mean temperature history associated with the particle types STS (green), NAT (blue) and ice (red). The shaded region shows ±1 standard deviation and the dashed lines show the 5^{th} and 95^{th} percentile

4.3 Time versus Temperature

This section examines the relative importance of the temperature at the time of observation and the amount of time a parcel has spent below a threshold in determining the type of PSC that will form. Figure 4.8 shows 2D histograms in which the temperature histories are binned according to their temperature below T_{NAT} at the time of the observation and total time spent below T_{NAT} - 4.5 K during the four days previous to observation. The bin size is 0.5 K by 6 hours, the smaller sized bins on either end of the 'time below' axis represent exactly 0 hours below T_{NAT} - 4.5 K and below T_{NAT} - 4.5 K for the entire four days. The threshold of T_{NAT} - 4.5 K was chosen as it results in the PSC observations being more evenly distributed across the four day range rather than being concentrated at either end. The slight top left to bottom right tilt of the distributions are due to the coupling between the variables, i.e. a history with a lower temperature at the time of observation is more likely to have been below a threshold temperature for a greater amount of time.

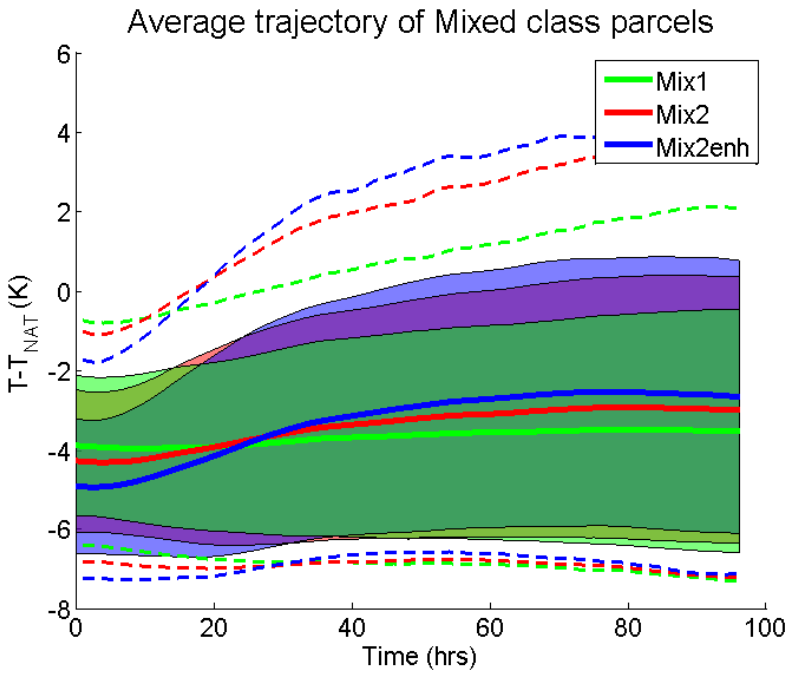

Figure 4.7: As for Figure 4.6 except showing Mix1 (blue), Mix2 (red) and Mix2enh (green)

The ability of temperature histories to discriminate between different PSC classes can be illustrated by showing the partitioning between two different PSC classes in each histogram bin. Figure 4.9 shows the percentage split been classes in each histogram bin for each combination of PSC classes. For the combinations involving the ice class the variables used are T-T_{ice} and time below T_{ice} + 2 K as it was found that this provided a clearer discrimination in these cases. As with the threshold in Figure 4.8, the T_{ice} + 2 K threshold was chosen to provide an even distribution across the range of times. The solid black line marks the contour where bins show a 50/50 split between classes, the dashed black line marks the 75/25 and 25/75 contours. The white contour encloses the region where the total number of trajectories within each bin is greater than average, this is important because a demarcation between the classes that occurs in areas where most of the histories are located in this space is more useful than a demarcation that only discriminates small fractions of one of the PSC classes. This distinction is however less important when comparing combinations that include the 'none' class as the number of observation of this class is much higher than other classes. Bins in which there are less than 100 trajectories in total are shown as blank.

Examination of Figure 4.9 indicates that the clearest discrimination is between the ice and Mix1 class, observations with temperatures below T_{ice} - 1 K are almost exclusively ice and above T_{ice} + 2 K are Mix1, the intervening range exhibits a time dependency where histories in which the temperature has been below the T_{ice} + 2 K threshold for longer are increasingly more likely to be Mix1, even observations that are below the frost point are equally likely to be Mix1 if the air parcel has spent over three days below T_{ice} + 2 K. This transition is not as narrowly constrained in the comparison between

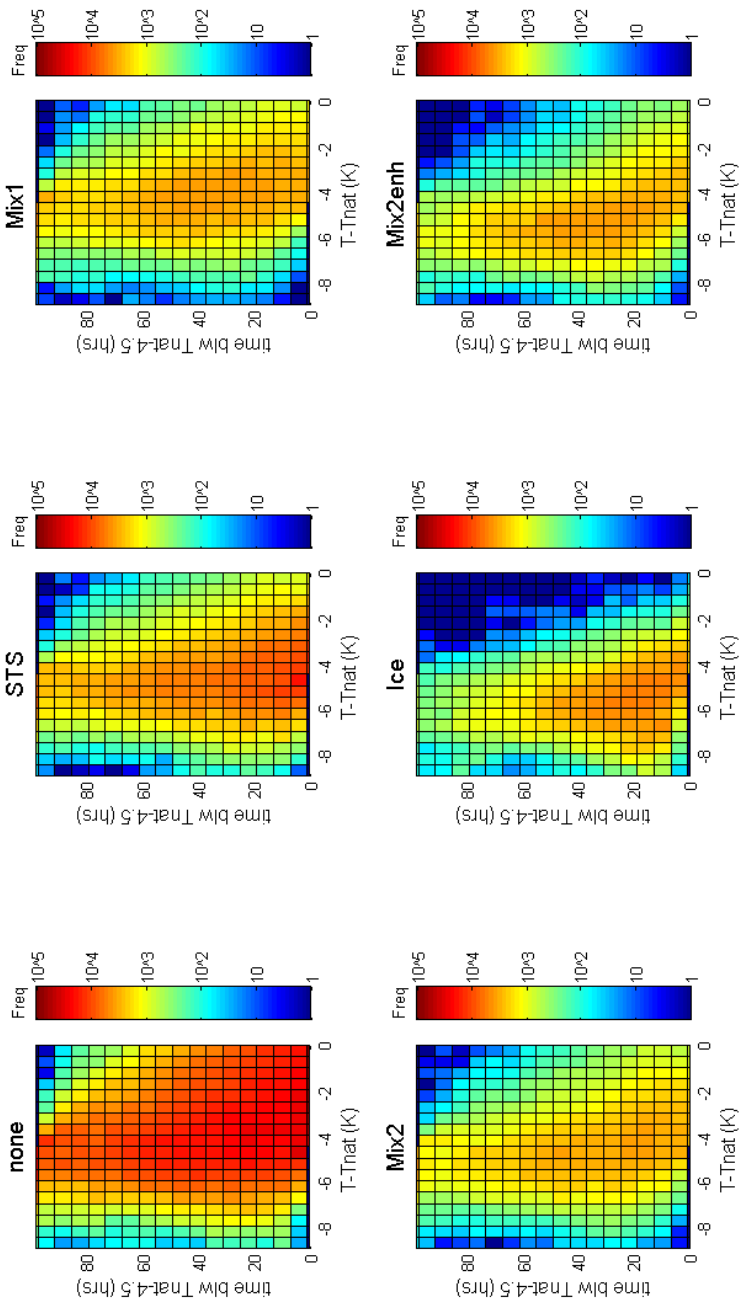

Figure 4.8: 2D histogram of showing the occurrence of the PSC class in terms of T-T$_{NAT}$ at the time of observation and the amount of time spent below T$_{NAT}$

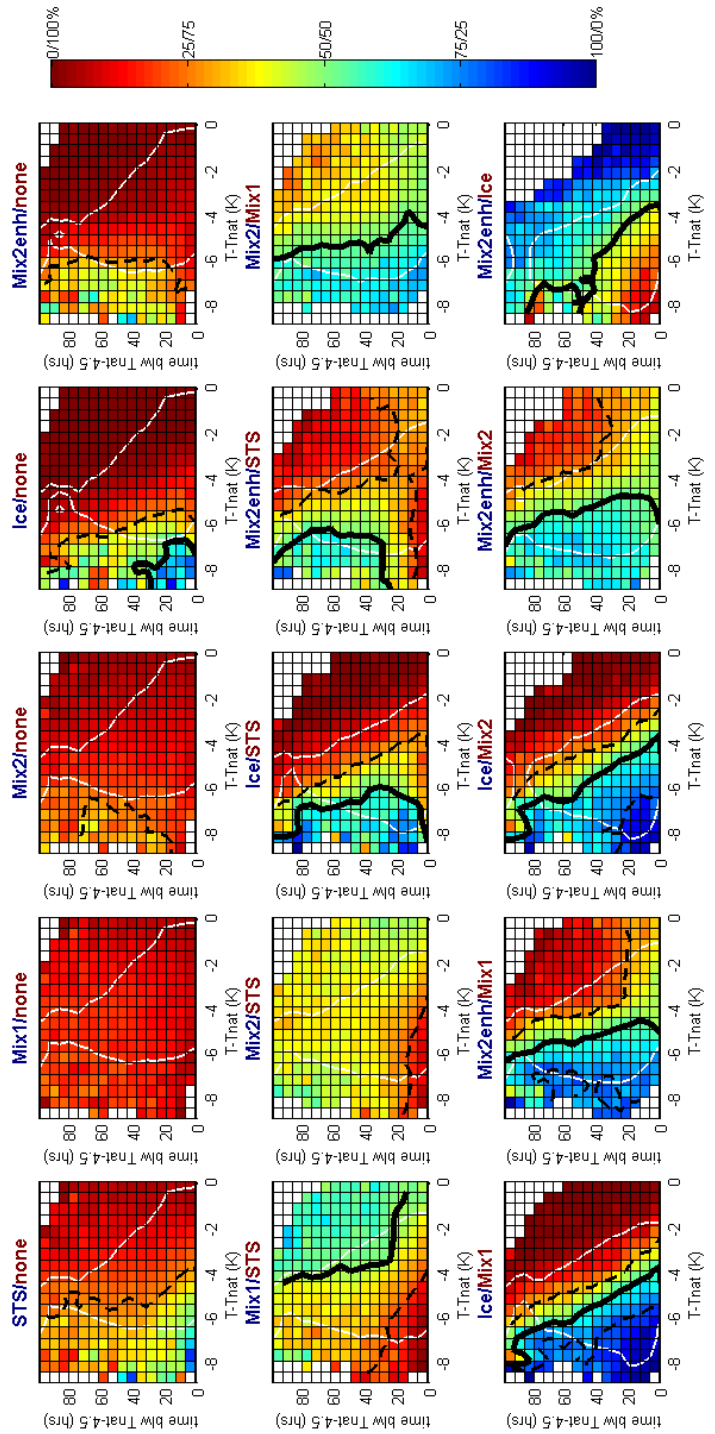

Figure 4.9: Partitioning between each combination of CALIOP class using temperature and time below a temperature threshold bins from Figure 4.8; the solid black line is the 50/50 contour, the dashed black lines are the 25/75 and 75/25 contour, the white curve encloses the bins for which the number of trajectories included in the bin is higher than average

Mix2 and ice and even less so in the Mix2enh/ice comparison. The fact that an air parcel that is observed at a temperature close to the water ice frost point is increasingly less likely to be observed as ice the longer it has experienced colder temperatures is somewhat counter-intuitive. This is possibly explained by sedimentation; if an air parcel experiences low temperatures for long time periods the ice particle may grow to a size where it falls from the air parcel's trajectory before the observation is made.

The discrimination between PSC and no PSC is generally not very clear. The clearest, unsurprisingly, is ice where the comparison shows that observations of ice become more favourable around 1 K below T_{ice}. The comparisons STS and Mix2enh with 'none' show some instances where these classes are around 50/50 or greater, namely temperatures below T_{NAT} - 6 K and times of less than a day in the case of STS and T_{NAT} - 6 K and times of greater than a day in the case of Mix2enh. In the comparisons between 'none' and Mix1 and Mix2 there are no bins which indicate a better than 50% probability of occurrence.

In comparing STS with the mixed classes in can be seen that regions that have been cold for a shorter amount of time are almost exclusively STS. However in all other regions, and particularly the more populous regions, the partitioning between the classes is more evenly split. In the less populous regions, the comparison shows Mix1 is slightly more favoured in histories where the temperature is above T_{NAT} - 4.5 K at the time of observation but has been below this threshold for longer than a day over the course of the trajectory, although the comparison with Mix2enh reveals that the same region favours the observation of STS while Mix2enh observations are more favoured if the current temperature is below T_{NAT} - 6 K and has been below T_{NAT} - 4.5 K for longer than 40 hours.

The comparison of Mix1 and Mix2 illustrates very little discrimination with only a slight tendency for Mix2 to be observed at lower temperatures and Mix1 to be observed at higher temperatures. Of course this is not surprising given the similar make up of the class, with Mix2 only being separated by a greater abundance of NAT than Mix1. To a lesser degree the same is true for the comparison between Mix2 and Mix2enh, this time with Mix2enh being slightly favoured at low temperatures.

4.4 The Role of Ice in NAT Formation

In order to investigate the role of ice in the formation of NAT the proportion of each PSC category present in each cloud was examined. For this analysis a 'cloud' is taken to be a length of uninterrupted positive PSC observations along the path of the satellite between the height range 18 to 22 km (chosen to coincide with the 450 K isentropic level). Only clouds with greater than 100 individual PSC observations are considered. The number of observations of each class within this height range is then determined for each cloud. The clouds are divided into two sets according to the presence of ice (where

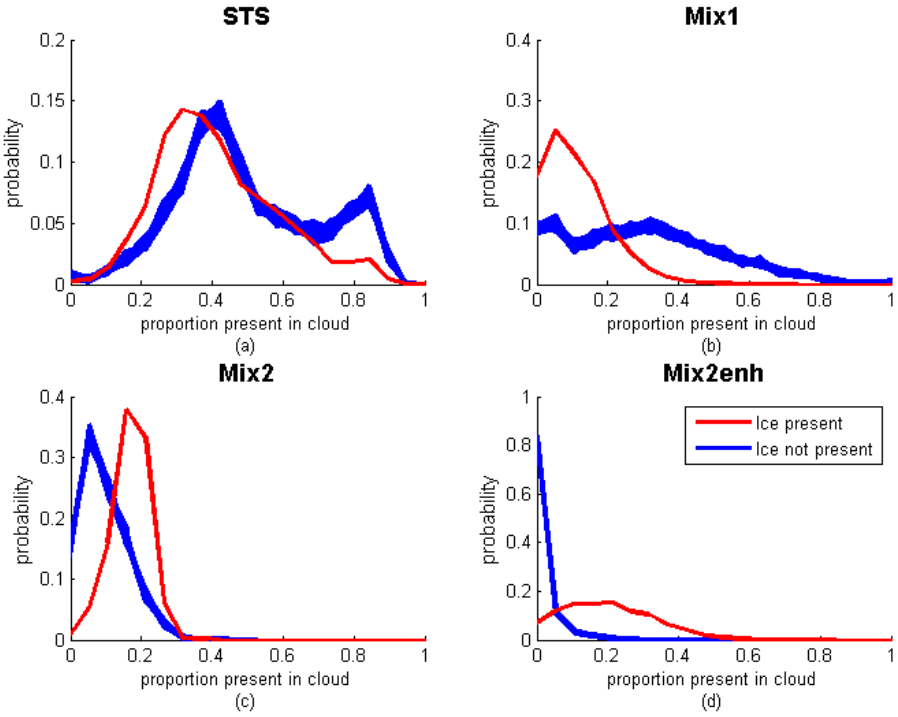

Figure 4.10: Proportion of (a) STS, (b) Mix1, (c) Mix2, and (d) Mix2enh in clouds containing ice (red) and not containing ice (blue)

ice constitutes >1% of the cloud) or its absence. The proportions of the constituents in the clouds containing ice are calculated with respect to the remainder (i.e. non-ice portion) of the cloud, so that the actual quantity of ice has no impact on the results. Figure 4.10 shows the probability density functions (PDFs) of the proportion of each PSC type in a cloud for both the ice present and absent situations. On average clouds containing ice are 1 - 2 K colder than those in which ice is absent, which potentially causes a sampling bias this is corrected for by sampling the non-ice clouds non-uniformly. Thus, the analysis presented in Figure 4.10 allows us to unambiguously identify whether the presence of ice PSC has an impact on the occurrence of other PSC types within the same cloud. To remove the sampling bias, the clouds are binned according to their mean temperature (over the length of the cloud at the 450 K level) and the non-ice clouds are randomly sampled from each 0.5 K bin, the number from each bin is chosen to match the amount of ice-containing clouds in that same bin. Thus, the distribution of mean temperature of clouds containing no ice will be the same as the distribution of the clouds that contain ice. The results of 20 different random samplings are shown in blue in Figure 4.10.

The most obvious feature of Figure 4.10 is the difference in Mix2enh abundance between ice present and absent clouds (see Figure 4.10(d)), where ice is absent there is scarcely ever any more than 10% Mix2enh in the cloud, but as much as 40% in clouds which contain ice PSC. To a lesser degree this effect is evident for the Mix2 portion of cloud (see Figure 4.10(c)), with ice present there is on average 20% Mix2 which falls to 10%

without ice. However in the case of Mix1 there is a lower abundance with the presence of ice (less than 40%) than without (as much as 80%). The oppositely orientated variations between Mix1 and Mix2 suggests that the presence of ice increases the quantity of NAT which means Mix2 becomes more likely to be observed at the expense of Mix1. The increased quantity of NAT observed in the presence of ice clouds suggests that the NAT formation by vapor deposition on ice mechanism [Luo et al. 2003; Wofsy et al. 1990] is likely to be an important mechanism for NAT formation. Although, as Luo et al. [2003] notes this mechanism does not explain the low number density NAT observations which concurs with the result from Figure 4.10(b) that Mix1 exists in greater abundance without the presence of ice. Therefore, it would there needs to be an additional formation mechanism that explains the existence of Mix1 observations. Figure 4.10(d) shows that generally there is little effect on the proportion of STS contained in the cloud; however there is a population of non-ice clouds for which STS constitutes around 85% of the cloud which is not present when looking at the set of clouds containing ice.

4.5 Recently Formed PSC

Looking at the entire four day temperature history for characteristics such as cooling rates is somewhat limited in that it is unknown a what point along the back trajectory the formation of the PSC occurred. In this section the range of trajectories is narrowed down to those where it can be shown that formation has occurred within the previous two days. Such trajectories are selected by looking for points along the back trajectory that coincide with a CALIOP measurement showing no PSC; 'coincident' is defined as within 300 km. Even with such a broad definition of coincidence very few of these trajectories are found, of the approximately seven million trajectory less than 20000 fit the criteria; this is due the orbit of the CALIPSO satellite being orientated in such a way with respect to the polar vortex that the satellite is usually moving in the opposite direction to a given air parcel (as was the case for the Aura MLS satellite, described in section 3.4). On average the time between observations along these trajectories was 33 hours.

Figure 4.11 shows the mean rate of cooling $\Delta T/\Delta t$ between the observations along the trajectory; separate cooling rate distributions are shown for each PSC class. The distribution of the Mix1 class is centred on zero, this agrees with the mean temperature history shown in Figure 4.7. All the other PSC classes skew towards positive cooling rates. Predictably ice shows the highest cooling rates, the mean cooling rate of the formation part of the ice temperature history is 0.17 K/hour. This value concurs with the mean cooling rate of the entire sample of ice temperature histories as shown in Figure 4.6. The mean cooling rate of the PSC classes is displayed in Table 4.1 as well as the percentage of trajectories for each class that exhibit positive cooling rates. The ice trajectories almost exclusively exhibit cooling prior to observation indicating that it is likely that cooling rates are a factor in ice formation, this is also true for Mix2enh (in

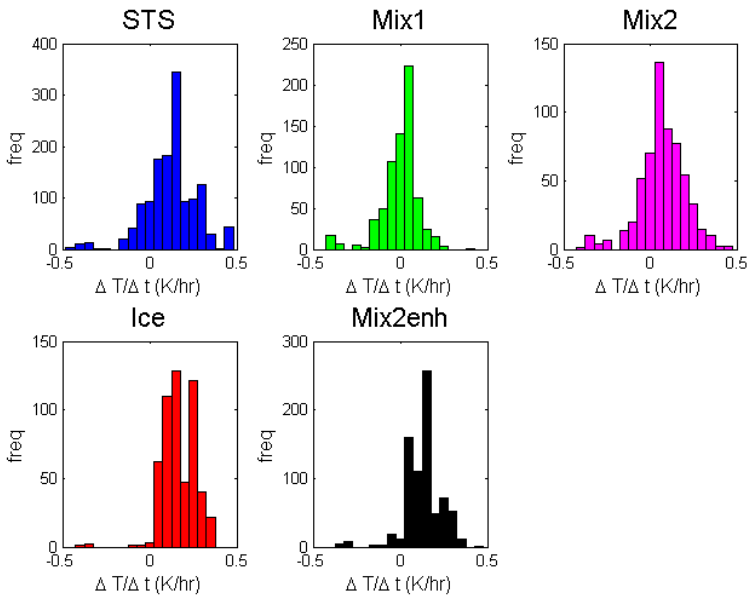

Figure 4.11: Distribution of mean cooling rates (negative is warming) over the period of the history in which particle formation has been isolated

95% of cases) but less so for Mix2 and STS for which only 76 and 83% of trajectories exhibit cooling prior to observation.

PSC Class	Mean cooling rate	% of traj. with +ve cooling rate
STS	0.12	83
Mix1	0.00	53
Mix2	0.07	76
Mix2enh	0.13	95
Ice	0.17	99

Table 4.1: Mean cooling rates over the portion of the temperature history associated with particle formation

4.6 Microphysical Model

The microphysical model for PSC formation described in section 3.5 was used to run simulations on 100 temperature histories; the model runs were obtained from Andrew Klekociuk. This sample of histories was selected from the 2007 PSC season and includes mostly trajectories in which PSC formation was anticipated to have occurred within the two days previous to the observation (identified using the methodology described in section 4.5). The initial H_2O and HNO_3 mixing ratios in the model were set at 4.5 ppmv and 8 ppbv, respectively; these are typical values prior to any dehydration or denitrification. The atmospheric mixing ratios in the model are allowed to vary based on uptake of the water vapour or nitric acid by particles, this differs from the approach taken in the rest of this thesis in which mixing ratios are prescribed from regional averages.

Comparison between the presence of particular PSC types in the model and CALIOP measurements highlights some interesting factors. In particular, the most significant difference between the predictions made by the model and the CALIOP observations was the underestimation of the abundance of NAT; only in 29% of the histories where CALIOP indicated the presence of NAT did the model show the presence of NAT at the time of observation. The mechanism of NAT production predominantly simulated by the model was initial formation of ice by cooling to temperatures at least 2 K below T_{ice} followed by melting of the ice as temperatures increase back over T_{ice}. The model also allows for the nucleation of NAT on SAT particles however this was not observed for any of the examined histories. the disparity between the model and the observations seems to suggest that there is another formation mechanism in addition to the mechanisms included in the model that is required to produce the correct amount of NAT. In contrast, the model over-predicts the abundance of ice, of the 18 instances where the model predicts the presence of only ice only three show observations of ice by CALIOP, the others are identified as observations of the mixed classes.

Errors in the estimation of the initial mixing ratios are likely the cause of some of the over-prediction of ice. In dehydrated regions the mixing ratio of water vapour decreases to around 2 ppmv, at a pressure of 50 hPa this represents a decrease in T_{ice} from 187.7 K (with 4.5 ppmv water vapour) to 183.2 K. Various other model settings may also have some effect.

4.7 An Improved Prescription for PSC Occurrence

The previous sections suggest ways in which the traditional temperature threshold type PSC proxies may be improved upon. This section takes some of these ideas and uses them to produce a categorization algorithm for temperature histories that aims to better predict PSC occurrence. Temperature histories are grouped into the categories A, B, C, D, and E in a hierarchical manner i.e. temperature histories selected in category A are not considered for category B.

Category A is designed to select temperature histories that form ice particles. This category includes temperature histories that either nucleate ice by supercooling with respect to T_{ice} or have a large cooling rate prior to observation. The supercooling criterion requires that the air parcel must cool to at least 2 K below T_{ice} at some point along the trajectory and then stay below T_{ice} after this point until the time of observation. The magnitude of supercooling required is chosen to be a middle-ground between results identified in Fortin et al. [2003] and Chang et al. [1999], namely ice nucleates on SAT at supercoolings of 0.1 - 1.7 K and STS freezes at supercoolings of 3 K. This behavior mimics that of the microphysical model [Larsen 2000]. The second criterion selects temperature histories which cool 7 K or more from the mean temperature over the t = 96 to t = 48 hour period in the temperature history compared to the temperature at t = 0; the temperature at t = 0 must also be below T_{ice}. This criterion

was instituted as large coolings in the recent history were characteristic of ice formation as shown by Figure 4.6 and the analysis detailed in section 4.5. A fall in temperature of 7 K over two days corresponds to an average cooling rate of 0.145 K/hour this falls in-between the mean rate of ice (0.17 K/hour) and the next largest mean rate, that of Mix2enh (0.13 K/hour).

Category B is designed to select temperature histories that form NAT particles via nucleation on ice particles. Temperature histories in this category have at some point formed ice as defined in category A and remained below T_{NAT} after this point. Figure 4.10 shows that the presence of ice particles increases the probability of occurrence of the Mix2 and Mix2enh classes so it may be expected that this category contains a high proportion of temperature histories associated with these classes.

Category C is designed to select temperature histories that form NAT particles without the aid of ice nuclei, most likely the Mix1 class. Figure 4.7 shows that in particular Mix1 temperature histories are characterized by persistent low temperatures. Figure 4.9 indicates that discriminating Mix1 from 'none' cannot be done effectively with simple temperature criteria, therefore the best that can be achieved is to discriminate Mix1 from STS and accept that this category will inevitably include a sizable fraction of clear observations. The Mix1/STS ratio from Figure 4.9 shows a region in which Mix1 observations are more likely, however this region exist mostly outside of the most populous part of the distribution. In order to select enough histories to model a realistic abundance of NAT the criteria was set at: below T_{NAT} - 4.5 K for in excess of 36 hours and above T_{NAT} - 5 K at the time of observation.

Category D is designed to select temperature histories that form STS. The criterion for this category is entirely empirical and is based on the 'STS/none' ratio diagram from Figure 4.9. Temperature histories selected in this category are those for which the following inequalities are true:

$$T < T_{NAT} - 4 - \frac{t_{below}}{24}$$

and

$$t_{below} < 48$$

where T is the temperature in K at the time of observation and t_{below} is the total time spent below T_{NAT} - 4.5 K in hours.

Category E contains all remaining temperature histories; it is expected that the majority will be temperature histories associated with clear observations.

Figure 4.12 shows the results of the categorization of the temperature histories in terms of the CALIOP class associated with each trajectory, the number of each CALIOP class in each category is grouped by category in Figure 4.12(a) and grouped by class in Figure 4.12(b). The quantity of clear observations is displayed reduced by a factor of 10 and

wave ice increased by a factor of 100 for clarity.

The most apparent feature of Figure 4.12(b) is the large amounts of PSC observations, particularly STS and the mixed classes, that get included in category E - where ideally there should be none. Figure 4.9 illustrated the difficulty in discriminating these classes from observations of no PSC based on the temperature history so it is unlikely that this problem can be avoided while still simulating a realistic abundance of each category. Ice and wave ice have less category E histories; they are primarily made up of category A and D temperature histories. In some cases the ice class may be a mixture of ice and STS [Pitts et al. 2009], this may explain why some of the ice observations are associated with category D. As designed, the most populous PSC classes in categories A and D were ice and STS, respectively. Categories B and C, designed to detect NAT mixture formation, however select more STS than any of the individual mix classes. There is a relatively large amount of 'none' in each of category B through D where, ideally, there should be very little.

The effectiveness of this categorization scheme may be examined by comparing it to the traditional temperature threshold scheme i.e. ice expected below T_{ice}, STS and NAT expected between T_{ice} and T_{STS}, NAT expected between T_{STS} and T_{NAT} and nothing expected above T_{NAT}. Table 4.2 shows the PSC composition in each of these temperature regimes. For the purpose of comparison the same statistics are shown for the trajectory categorization in Table 4.3. The wave ice class is not shown as it constitutes less than 0.25% in all cases.

The temperature history categorization is a modest improvement over the temperature threshold scheme. Category A, by virtue of its more restrictive criteria, has a higher portion of ice observations, 28% as compared to 17%, than its equivalent in the temperature threshold scheme ($T < T_{ice}$). This increase is primarily due to by a similar sized decrease in the proportion of clear observations; Mix2enh also shows a small increase with decreases in Mix1 and STS. Category D has a slightly higher proportion (23%) of STS observations as the $T_{ice} < T < T_{STS}$ regime (although evaluating based on this comparison is not fair as it is entirely possible for NAT to exist in this temperature regime) but with a lower proportion of clear observations (44%, as opposed to 55%). The temperature regime in which only NAT is expected ($T_{STS} < T < T_{NAT}$) contains mostly (73%) clear observations, the corresponding categories (B and C) have higher compositions of each of the mixed observation which come with a lower proportion of clear observations (57 and 64%, respectively). Thus, on the whole the improved class discrimination within the categories is facilitated by more stringent criteria, the side effect of which is that more temperature histories fall into category E, there are 4.9 million temperature histories in this category compared to 2.3 million in the $T > T_{NAT}$ regime. Of coarse, this abundance of trajectories where no PSC is expected is desired given that the most important problem with the temperature threshold scheme was that it over-estimated PSC occurrence; however, this does result in a lower proportion of temperature histories in this category correctly identified as having no PSC (85%, as

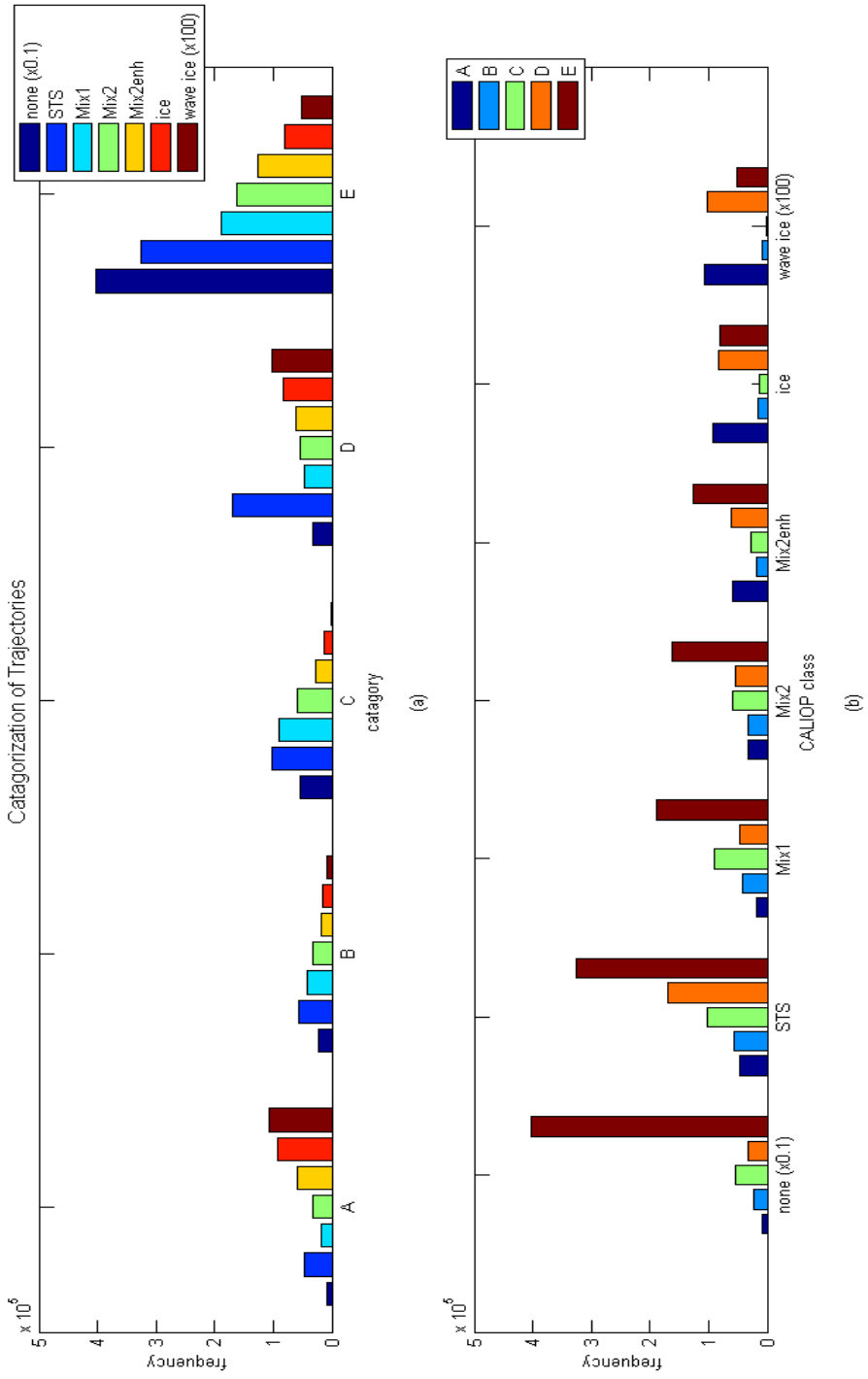

Figure 4.12: Categorization of temperature histories in terms of their associated CALIOP class measurement

compared to 98% of observations with $T > T_{NAT}$ being identified as 'none').

	CALIOP Class (%)						Tot. Traj.
	none	STS	Mix1	Mix2	M2e	Ice	(1000's)
$T < T_{ice}$	35	16	8	10	14	17	1169
$T_{ice} < T < T_{STS}$	55	20	9	7	4	4	1322
$T_{STS} < T < T_{NAT}$	73	10	7	5	3	2	2410
$T > T_{NAT}$	98	1	1	0	0	0	2336

Table 4.2: Composition of each temperature regime delineated by the threshold temperature thresholds T_{ice}, T_{STS}, and T_{NAT}

	CALIOP Class (%)						Tot. Traj.
	none	STS	Mix1	Mix2	M2e	Ice	(1000's)
A	25	14	6	10	17	28	336
B	57	15	11	8	5	4	385
C	64	12	11	7	3	2	824
D	44	23	6	7	8	11	752
E	85	7	4	3	2	2	4916

Table 4.3: As for 4.2 except for trajectory categories

The categorization scheme can be evaluated further by examining the mean temperature histories of each CALIOP class in each temperature history category; these are shown in Figure 4.13 with category A in terms of T - T_{ice} and the others in terms of T - T_{NAT}. If the temperature history of the targeted class within a category differs by only a small amount from the other classes this is indicates that further adjustments to the temperature history are unlikely to result in better discrimination of the targeted class. In category A the mean ice temperature history is distinguished by having the largest cooling rate prior to observation. This suggests that it may be possible to further improve the ice discrimination in this category by modification of the cooling rate criterion, although as category A is the combination of two criteria this is not guaranteed to be the case. Category B was expected to select mainly Mix2 and Mix2enh temperature histories; however, Figure 4.12(a) shows there are large portions of clear, STS, and Mix1 in this category; Figure 4.13 shows that on average the temperature minima of the Mix2 and Mix2enh histories occur closer to the time of observation than is the case for 'none' and Mix1. It possible that the discrimination of the Mix2 and Mix2enh classes by this category could potentially be improved by accounting for this phenomenon, although it may also be possible that this phenomenon is just a statistical artifact as the physical reason that the timing of the minima should effect the class of observation is not apparent. Category C is designed to select mostly Mix1; however, 64% of this category is composed of clear temperature histories. Figure 4.13 shows that the temperature histories of clear and Mix1 are very close in categories A to C and, to a lesser degree D, meaning improvements in the discrimination between these two classes are unlikely to be found. In category D the mean STS history is distinguished by a slightly higher temperature for times in excess of a day previous to the observation and hence faster cooling rates prior to the observation. It is conceivable that cooling rate may make some

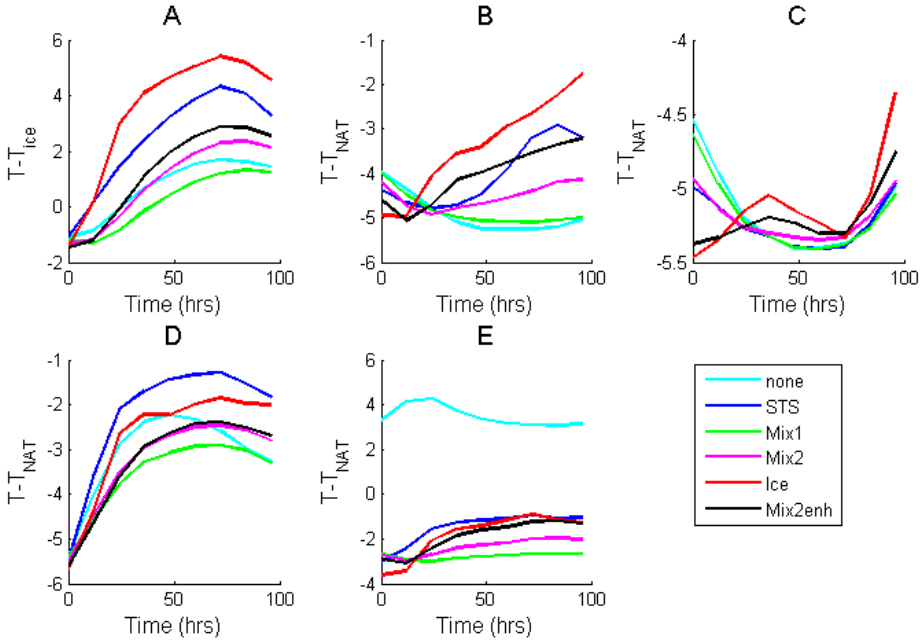

Figure 4.13: Mean temperature histories of each CALIOP class in each temperature history category

small difference to the probability of STS observation based on the findings of Meilinger et al. [1995] described in section 2.7. As expected the mean clear trajectory in category E is significantly warmer than the other classes.

The temperature history categorization and temperature threshold schemes can also be compared geographically. Figure 4.14 shows the coverage of PSC observed by CALIOP, Figure 4.15 the coverage predicted by the temperature history scheme (i.e. the sum of all categories A to D), and Figure 4.16 the coverage predicted by temperature threshold (i.e. all measurements with $T < T_{NAT}$). The coverage is calculated by finding the fraction of data that are observed (or predicted) to be PSCs within 2.5° latitude by 10° longitude bins. The total areal coverage is calculated by summing the product of the fractional coverage of each bin and the area of each bin. The latitudinal extent of the bins is from 55°S to 82.5°S, the fractional coverage poleward of 82.5° is estimated as the average over the southern-most circle of bins; as temperatures typically continue to decrease toward the pole this is may be an under-estimate of actual PSC coverage; this region is indicated in the figures by a black dashed line.

As indicated in chapter 1, the T_{NAT} temperature threshold criterion represents a large over-estimation of PSC coverage. For the 2007 - 2010 seasons the area covered by PSC as observed by CALIOP is 7.6 million km^2, while the area with temperatures below the threshold is 20.4 million km^2. The area estimated via temperature history categorization is an improvement over this, but is still an over estimation at 8.6 million km^2. Around the perimeter of the continent the prediction seems to provide a good approximation, while the over-estimation occurs primarily at high latitudes where the PSC fractional coverage is observed to be around 0.5, while the prediction is around 0.7. This may

be due in part to the uncertainty associated with there being no CALIOP observations south of 82°, as noted previously the areal coverage is likely to be an under-estimate. While the overestimation of areal coverage based on the T_{NAT} threshold is large (a factor of 2.7 larger than CALIOP) it is possible to improve the estimate simply by adjusting the threshold. Pitts et al. [2009] suggests using T_{STS} as a threshold, this does indeed produce a better estimate, predicting an areal coverage of 8.7 million km^2 - similar in magnitude and geographic distribution to the category based prediction.

While the improvements in the total areal coverage made by the temperature history categorization can be reproduced more simply by adjusting the temperature threshold, the main advantage of categorization is that it allows the amount of the different PSC classes and their geographic distribution to be better simulated. This is important as the different PSC types activate chlorine at different rates as shown in Figure 1.5. Figures 4.17 and 4.18 show the individual components of Figures 4.14 and 4.15, respectively. The geographic distribution of the classes is relatively well simulated by the categories. Comparison of the distributions of ice and category A shows that the distribution is predicted accurately over the continent although, there is a small amount of ice observed around the perimeter of the continent which is not matched by category A. Also the map of category A shows that high concentrations extending into the Weddell Sea region which is characteristic of the distribution of Mix2enh in Figure 4.17. Suggesting that category A may be better suited as a proxy for both ice and Mix2enh rather than just ice. Category B and C model the extent of the Mix1 and Mix2 class relatively well. As category B is based on the 'NAT nucleation on ice mechanism' the good agreement between category B and Mix2 concurs with the findings of section 4.4 in which the presence of ice was found to increase the likelihood of Mix2 observations. Category C overestimates the abundance of Mix1, particularly over West Antarctica. Category C is more empirically based (as opposed to categories A and B which stem from theoretical ideas of formation mechanisms), which is perhaps why it does not correspond as well to the geographical distribution. The extent of STS observation is reasonably well matched by category D however, the coverage over West Antarctica is overestimated and somewhat under-estimated over East Antarctica. As with category C, category D is empirically based, perhaps explaining the errors in geographical distribution.

4.8 Discussion of Uncertainties

The most troublesome aspect of the current work is the large amount of observations showing no PSC that have either similar temperatures or temperature histories to observations which contain PSC. This may due to inaccuracies in one or more of the datasets used. The measurements of water vapour in the MLS dataset are believed to be relatively accurate, however the nitric acid measurements are quite noisy [Livesey et al. 2011]. Livesey et al. [2011] quotes the precision of the nitric acid measurement in the range 32 - 100 hPa as ± 0.7 ppbv and the uncertainty of the bias as ± 0.5 - 1ppbv.

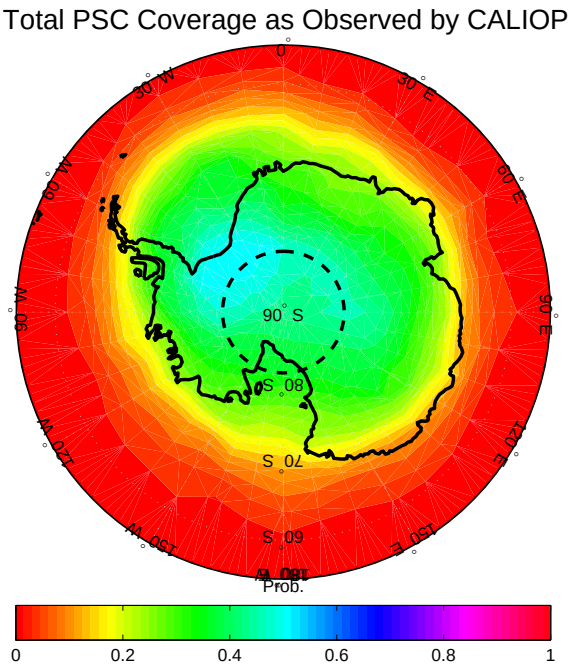

Figure 4.14: Coverage of PSC as observed by CALIOP over the 2007-10 PSC seasons

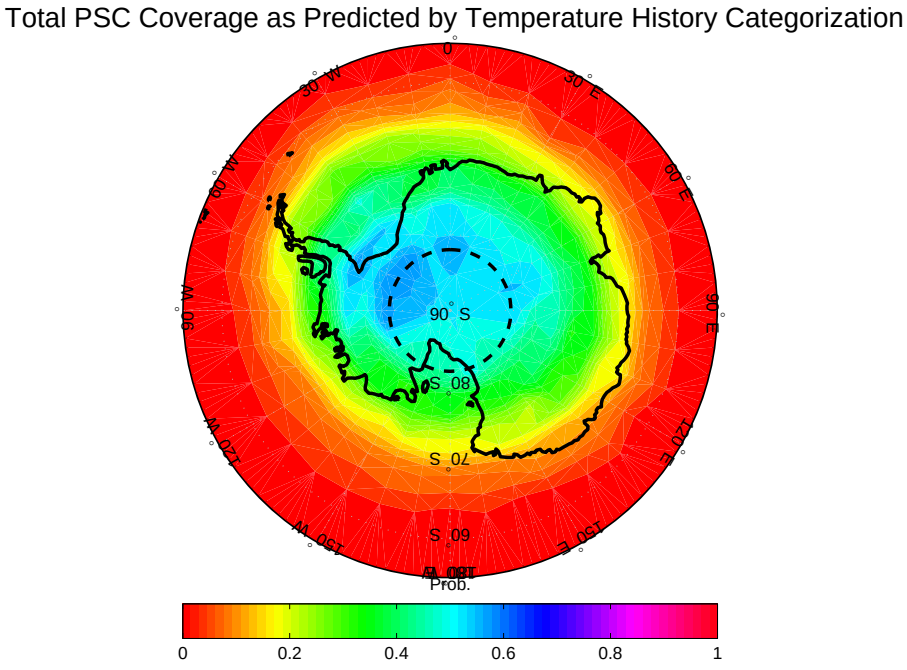

Figure 4.15: As for 4.14 but with predictions based on temperature histories

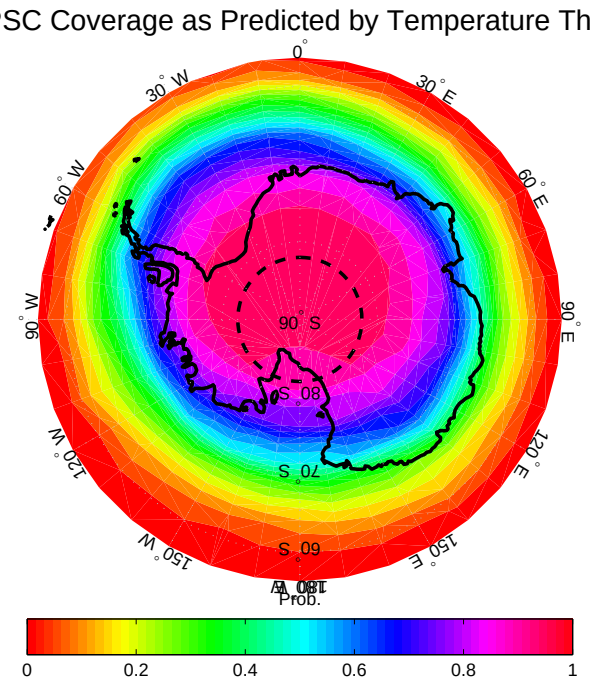

Figure 4.16: As for 4.14 but with predictions based on the temperature threshold T_{NAT}

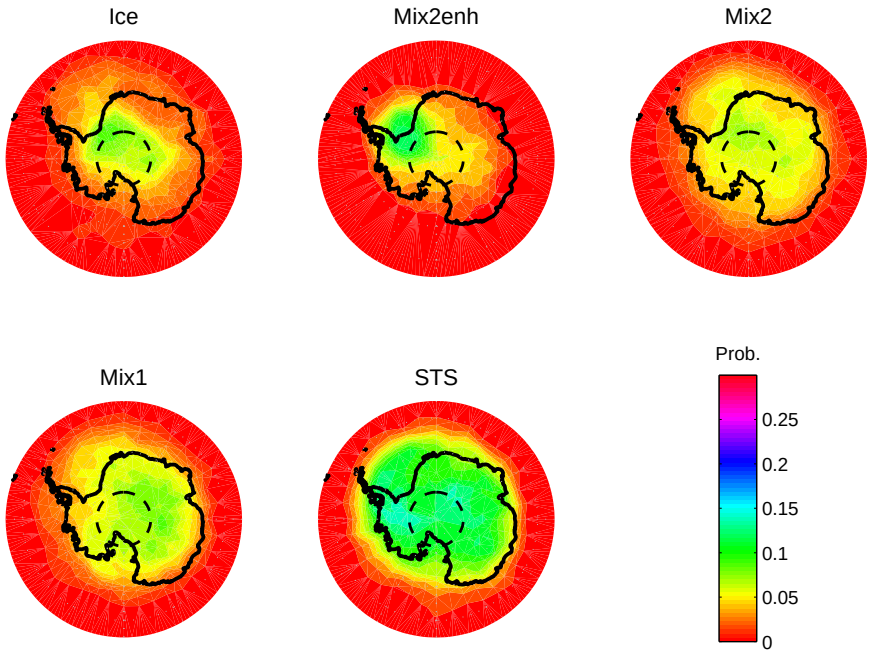

Figure 4.17: Coverage of individual PSC classes observed by CALIOP

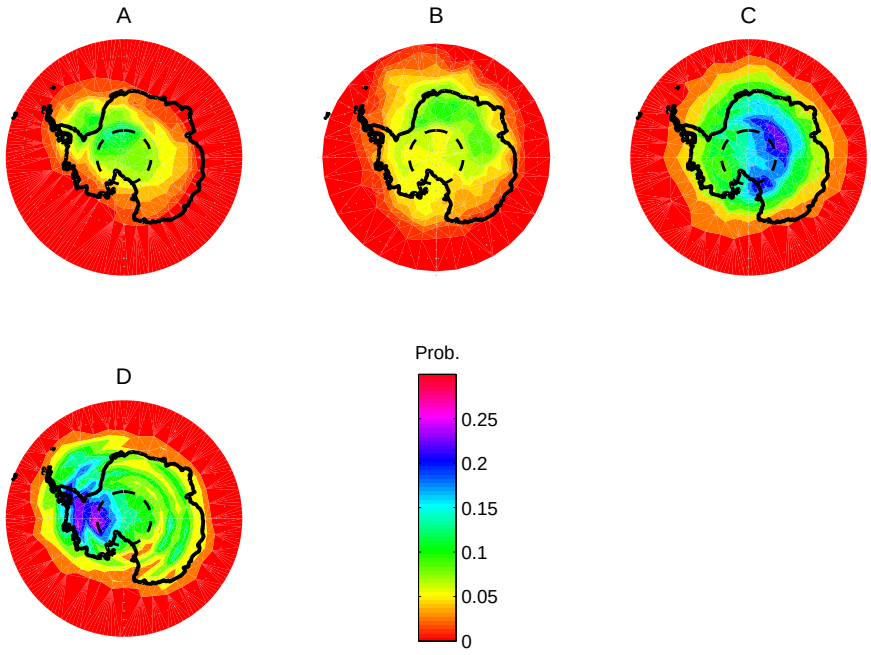

Figure 4.18: Coverage of the temperature history categories

The uncertainty in T_{NAT} resultant from a $\pm$ 1 ppbv uncertainty in HNO_3 at 50 hPa, a H_2O mixing ratio of 4 ppmv, and HNO_3 mixing ratio of 8 ppbv is $\pm$ 0.2 K, although this increases to around $\pm$ 2 K in heavily denitrified regions. The process of averaging the MLS data should mitigate some of the noise problem, although it may introduce another problem; because the bins are so large there may be regions with very localized nitric acid scarcity which will not be identified. This is particularly a problem at the edge of the denitrified region where the change in mixing ratio between adjacent bins can be as high as 4 ppbv (see Figure 3.2 for an example of this). Another explanation for this puzzling result could be that either the CAPIOP instrument or the algorithm used to detect PSC from the backscatter data fails to detect tenuous PSC, perhaps misclassifying what could be a STS or Mix1 observation as 'no PSC'. It is also possible that there may be biases in the MERRA data; most of the assimilated data is from surface or tropospheric observations and also most of the validation concerns these lower levels so it is reasonable to assume that the temperature and wind data from the stratosphere carries some amount of uncertainty.

Chapter 5

Conclusions and Future Work

The purpose of this research was to evaluate the effectiveness of temperature thresholds in predicting the occurrence of PSC and to investigate the influence of an air parcels temperature history on PSC occurrence. The most recent WMO ozone depletion report [WMO 2010] shows that using T_{NAT} as a temperature threshold produces a sizable over-estimate of the PSC coverage when compared to 2007 CALIOP observations (see Figure 1.1). A similarly sized over-estimation was found when comparing the areal coverage on the 450 K isentropic level over the June to September 2007-10 period (see Figure 4.14 and 4.16). Figure 4.2 shows that the three CALIOP classes containing NAT, namely Mix1, Mix2, and Mix2enh occur most frequently in regions where the temperature is 4 - 6 K colder than T_{NAT}. Therefore, T_{NAT} does not appear to be a good threshold for either PSC occurrence generally or NAT occurrence specifically. Other temperature thresholds do a better job at predicting the occurrence of particular PSC constituents. Figure 4.2 shows that the water ice frost point, T_{ice}, is a relatively good predictor of ice occurrence with the peak in the occurrence distribution just below T_{ice}, however 31% of the ice PSC observations did occur above T_{ice}, Pitts et al. [2012] attributes this to temperature perturbations caused by gravity waves although this may also be attributed to uncertainty in MERRA or MLS data. The temperature threshold of STS, T_{STS}, used in this study, was estimated to be T_{NAT} - 4 K based on the work of Carslaw et al. [1994]. The peak in observational frequency of STS was located slightly below T_{STS} and 36% of observations occurred above this threshold; this is due to the threshold being imprecisely defined, Figure 2.3 shows that STS rapid growth occurs over a range of around 2 K [Carslaw et al. 1994].

In order to examine the influence of the temperature history on PSC formation a four day long Lagrangian back trajectory was calculated from the location of each CALIOP observation on the 450 K isentropic level. Over the June to September period from 2007 to 2010 this amounted to over seven million trajectories. The temperatures were interpolated from MERRA data at each hourly increment along the trajectory. H_2O and HNO_3 concentrations were assigned at the same increments from a spatial and temporal average of MLS data for the purpose of calculating T_{NAT} and T_{ice}.

It was found that there was a marked difference in the behaviour of the temperature histories associated with ice particles and those of the NAT classes (see Figures 4.4, 4.5, 4.6 and 4.11). Ice temperature histories are characterized by a large temperature drop, on average 4 K, over the 24 hours prior to the observation. For times more than 24 hours previous to the observation the temperature distribution of the ice trajectories is indistinguishable from the climatological temperature distribution. On the other hand NAT temperature histories, particularly the Mix 1 class, are characterized by having maintained cold temperatures for long periods of time, typically staying below T_{NAT} for the entire four day history. In contrast to ice temperature histories which almost exclusively exhibit cooling prior to observation, Mix1 histories are just as likely to exhibit warming prior to observation as they are to exhibit cooling (see Table 4.1). In this respect Mix2enh histories are similar to ice, exhibiting cooling on 95% of the occasions where formation could be shown to have occurred within the two days prior to the observation.

Given the incidence of NAT at cooler temperatures and the existence of mechanisms for NAT formation linked to ice, the effect of the presence of ice on the occurrence of NAT was investigated by examining CALIOP class composition of large scale clouds (see section 4.4). It was found that the vast majority of the Mix2enh class occurs in the presence of ice, the presence of ice also increases the amount of Mix2. This would seem to support the formation theory in which NAT nucleates on existing ice particles [Luo et al. 2003; Wofsy et al. 1990]. Mix1, on the other hand, exists in greater abundance without the presence of ice, therefore an additional NAT formation mechanism is likely required to explain these observations. The occurrence of STS is generally not effected by the presence of ice (see Figure 4.10). The overall geographic distribution of the classes seems to concur with these findings (see Figure 4.17). The ice, Mix2enh and, to a lesser degree Mix2 distributions are concentrated in the region inland from the Weddell Sea; Mix1 typically occurs down stream of this region.

An algorithm was proposed for categorizing the temperature histories in order to predict the occurrence of the different PSC types. The algorithm includes some findings from the literature such as the supercooling requirements for ice formation [Chang et al. 1999; Fortin et al. 2003] and empirical aspects derived form the temperature history database, such as the ability to discriminate between PSC classes based on the combination of the temperature at the time of observation and the time spent below a temperature threshold over the course of the history (see Figure 4.9). While the discrimination between classes on a trajectory by trajectory basis achieved by the temperature history categorization was somewhat better than that achieved by the traditional temperature thresholds (see Tables 4.2 and 4.3) there is still a large amount of miscategorizaion (see Figure 4.12). However, the benefit of simulating PSC occurrence based on temperature history categorization can be seen by comparing the total areal coverage and geographic distribution of the observed and simulated PSC (see Figures 4.14 to 4.18). The average observed areal coverage over the period examined was 7.6 million km^2, while the area simulated based on the temperature history categories was 8.6 million km^2 - which is

much better than the prediction of 20.4 million km^2 made by using T_{NAT} as a proxy. Also, the geographical distributions of the individual categories generally match well with the individual CALIOP classes that they aim to simulate; this is important as the different PSC types activate chlorine at different rates (see Figure 1.5). The categorization algorithm was subject to only a nominal amount of tuning, it is possible further adjustment could provide improvements in the discrimination between the PSC classes but this would require much extra work outside the scope of this thesis. It may also be interesting to examine an entirely empirical categorization scheme based on an approach similar to that illustrated in Figure 4.9.

The largest problem faced in predicting the formation of PSC based on the temperature history was the amount of histories associated with observations of no PSC that had the same characteristics as those associated with observations of PSC (see Figure 4.9). It is possible this problem is due to uncertainty in the datasets or the averaging process in the case of the MLS data. The largest source of uncertainty is expected to be due to the MLS HNO_3 mixing ratio data. HNO_3 (as well as the H_2O) mixing ratios were averaged over 5° latitude by 30° longitude by 7 days bins; however, Figure 3.2 shows that using bins of this size mean that the change in the mixing ratio between adjacent bins is relatively large. This implies that the uncertainty of T_{NAT} is quite large; however due to the sparsity of the MLS data this problem is impossible to avoid.

An alternative approach to examining the effect of temperature history that avoids the issues associated with having to average the MLS data would be to calculate a forward trajectories originating from the locations of MLS measurements and running the microphysical model on the temperature history using the measured H_2O and HNO_3 as initial values in the simulation. The output of the microphysical simulation could then be compared to some regional average of the CALIOP observations located at the end of the trajectory. Of course, there will still be some uncertainty in T_{NAT} associated with the precision of the HNO_3 mixing ratios, which could be as high as ± 2 K (see section 4.8). This approach may also be limited due to the time it takes to run the microphysical model on each temperature history (~15 min); however, this study only briefly examined the use of the microphysical model, so it would be interesting to examine this more in future work.

Another good next step in this research would be to integrate the temperature history calculation scheme with a model of ozone chemistry, such as the empirical model described in Huck [2007]. The differentiation between the different PSC particle types with their different rates of chlorine activation ought to make the modeling of ozone destruction more accurate. Such a model could also be used to predict the future behaviour of the ozone hole using output from GCMs.

Bibliography

Adriani, A. et al., Climatology of polar stratospheric cloud based on lidar observations from 1993 to 2001 over McMurdo Station, Antarctica, *Journal of Geophysical Research: Atmospheres*, 109, 2004.

Ajtic, J. et al., Dilution of the Antarctic ozone hole into southern midlatitudes, 1998-2000, *Journal of Geophysical Research: Atmospheres*, 109, (D17), 2004.

Alexander, S. P. et al., The effect of orographic gravity waves on Antarctic polar stratospheric cloud occurrence and composition, *Journal of Geophysical Research: Atmosphreres*, 116, (D06109), 2011.

Arnold, F. et al., Evidence for stratospheric nitric acid condensation from balloon and rocket measurements in the arctic, *Nature*, 342, 493–497, 1989.

Biermann, U. M. et al., FTIR studies on lifetime prolongation of stratospheric ice particles due to NAT coating, *Geophysical Research Letters*, 25, (21), 3939–3942, 1998.

Browell, E. V. et al., Airboure lidar observations in the wintertime Arctic stratosphere: polar stratospheric clouds, *Geophysial Research Letters*, 17, (4), 385–388, 1990.

Burkert, P, F. Fergg, and H. Fischer, A compact high-resolution Michelson interferometer for passive atmospheric sounding (MIPAS), *IEEE Transactions on Geoscience and Remote Sensing*, GE-21, (3), 345–349, 1983.

Carslaw, K. S. et al., Stratospheric aerosol growth and HNO_3 gas phase depletion from coupled HNO_3 and water uptake by liquid particles, *Geophysical Research Letters*, 21, 2479–2482, 1994.

Chang, H. Y., T. Koop an L. T. Molina, and M. J. Molina, Phase transitions in emulsified HNO_3/H_2O and $HNO_3/H_2SO_4/H_2O$ solutions, *Journal of Physical Chemistry A*, 103, 2673–2679, 1999.

Chapman, S., A theory of upper atmospheric ozone, *Mem. Roy. Soc.* 3, 103–109, 1930.

Cox, R. A. et al., Activation of stratospheric chlorine by reactions in liquid sulphuric acid, *Geophysical Research Letters*, 21, (13), 1439–1442, 1994.

Drdla, K. and R. P. Turco, Denitrification through PSC formation: a 1-D model incorporating temperature oscillations, *Journal of Atmospheric Chemistry*, 12, 319–366, 1991.

Eckermann, S. D. et al., Antarctic NAT PSC belt of June 2003: observational validation of mountain wave seeding hypothesis, *Geophysical Research Letters*, 36, (L02807), 2009.

Fahey, D. W. et al., In-situ measurements of total reactive nitrogen, total water, and aerosol in polar stratospheric cloud in the Antarctic, *Journal of Geophysical Research: Atmospheres*, 94, (D9), 11299–11315, 1989.

Farman, J. C., B. G. Gardiner, and J. D. Shanklin, Large losses of total ozone in Antarctica revael seasonal CLOX/NOX interaction, *Nature*, 315, (6016), 207–210, 1985.

Fortin, T. J. et al., Ice condensation on sulfuric acid tetrahydrate: implications for the polar statospheric ice clouds, *Atmospheric Chemistry and Physics*, 3, 987–997, 2003.

Fueglistaler, S. et al., NAT-rock formation by mother clouds: a microphysical model, *Atmospheric Chemistry and Physics*, 2, 93–98, 2002.

Garney, H., G. E. Bodeker, and M. Dameris, Trends and variability in stratospheric mixing: 1979-2005, *Atmospheric Chemistry and Physics*, 7, 5611–5624, 2007.

Hanson, D. and K. Mauersberger, Laboratory studies of the nitric acid trihydrate: implications for the south polar stratosphere, *Geophysical Research Letters*, 15, 855–858, 1988.

Hertzog, A., P. Cocquerez, C. Basdevant, et al., Strateole/Vorcore - long-duration, superpressure balloons to study the Antarctic lower stratosphere during the 2005 winter, *Journal of Atmospheric and Oceanic Technology*, 24, 2048–2061, 2007.

Höpfner, M. et al., Spectrospic evidence for NAT, STS and ice in MIPAS infrared limb emission measurements of polar stratospheric clouds, *Atmospheric Chemistry and Physics*, 6, 1201–1209, 2006.

Huck, P. E. (2007), The coupling of the dynamics and chemistry in the Antarctic stratosphere, PhD thesis, University of Canterbury.

Iraci, L. T., A. M. Middlebrook, and M. A Tolbert, Laboratory studies of the formation of polar stratospheric clouds - nitric acid condensation on thin sulfuric acid films, *Journal of Geophysical Research: Atmospheres*, 100, (D10), 20969–20977, 1995.

Iraci, L. T., T. J. Fortin, and M. A. Tolbert, Dissolution of sulfuric acid tetrahydrate at low temperatures and subsequent growth of nitric acid trihydrate, *Journal of Geophysical Research: Atmospheres*, 103, (D7), 8491–8498, 1998.

Khosrawi, F. et al., Denitrification and polar stratospheric cloud formation during the Arctic winter 2009/2010, *Atmospheric Chemistry and Physics*, 11, 8471–8487, 2011.

Kim, Y. et al., Polar stratospheric clouds observed by the ILAS-II in the Antarctic region: dual compositions and variation of compositions during June to August of 2003, *Journal of Geophysical Research: Atmospheres*, 111, (D13S90), 2006.

Knopf, D. A. et al., Homogeneous nucleation of NAD and NAT in liquid stratospheric aerosols: insufficient to explain denitrification, *Atmospheric Chemistry and Physics*, 2, 207–214, 2002.

Koop, T. and K. S. Carslaw, Melting of $H_2SO_4.4H_2O$ particles upon cooling: implications for polar stratospheric clouds, *Science*, 272, 1638–1641, 1996.

Koop, T. et al., Do stratospheric aerosols droplets freeze above the ice frost point? *Geophysical Research Letters*, 22, 917–920, 1995.

Koop, T. et al., Freezing of $HNO_3/H_2SO_4/H_2O$ solutions at stratospheric temperatures: nucleation statistics and experiments, *Journal of Physical Chemistry A*, 101, 1117–1133, 1997b.

Koop, T. et al., A new optical technique to study aerosol phase transitions: the nucleations of ice from H_2SO_4 aerosols, *Journal of Physical Chemistry A*, 102, 8924–8931, 1998.

Koop, T. et al., Water activity as the determinant for homogeneous ice nucleation in aqueous solutions, *Nature*, 460, 611–614, 2000.

Lambert, A. et al., Validation of the Aura Microwave Limb Sounder stratospheric water vapour and and nitrous oxide measurements, *Journal of Geophysical Research: Atmospheres*, 112, (D24S36), 2007.

Larsen, N., *Polar stratosphric clouds: microphysical and optical models*, Danish Meteorological Institute, 2000.

Larsen, N. et al., Temperature histories in liquid and solid polar stratospheric cloud formation, *Journal of Geophysical Research: Atmospheres*, 102, (D19), 1997.

Livesey, N. J. et al., *Version 3.3 Level 2 data quality and description document.* Jet Propulsion Laboratory, California Institute of Technology, 2011.

Lowe, D. and A. R. MacKenzie, Polar stratospheric cloud microphysics and chemistry, *Journal of Atmospheric and Solar-terrestrial Physics*, 70, 13–40, 2008.

Luo, B. P. et al., Extreme NAT supersaturations in mountain wave ice PSC's: a clue to NAT formation, *Journal of Geophysical Research: Atmospheres*, 108, (D15), 2003.

MacKenzie, A. R. et al., On the theories of type 1 polar stratospheric cloud formation, *Journal of Geophysical Research: Atmospheres*, 100, (D6), 11275–11289, 1995.

MacKenzie, A. R. et al., Correction to: On the theories of type 1 polar stratospheric cloud formation, *Journal of Geophysical Research: Atmospheres*, 102, (D16), 19729–19730, 1997.

MacKenzie, A. R. et al., The Turnbull correlation and the freezing of stratospheric aerosol droplets, *Journal of Geophysical Research: Atmospheres*, 103, (D9), 10875–10884, 1998.

Marti, J. and K. Mauersberger, A survey and new measuremets of ice vapour pressure at temperatures between 170 and 250K, *Geophysical Research Letters*, 20, 363–366, 1993.

Masters, J., *Dr. Jeff Masters Wundergroud Blog*, URL: `http://www.wunderground.com/blog/JeffMasters/comment.html?entrynum=263`, Dec. 15, 2005date.

McCormick, M. P. et al., High-latitude stratoshperic aerosols measured by the SAM II satellite system in 1978 and 1979, *Science*, 214, (4518), 328–331, 1981.

McCormick, M. P. et al., Polar stratosphericcloud sightings by SAM II, *Journal of the Atmospheric Sciences*, 39, 1387–1397, 1982.

McDonald, A. J., S. E. George, and R. M. Woodlands, Can gravity waves signicantly impact PSC occurrence in the Antarctic? *Atmospheric Chemistry and Physics*, 9, 8825–8840, 2009.

Meilinger, S. K. et al., Size-dependent stratospheric droplet composition in lee wave temperature fluctuations and their potential role in PSC freezing, *Geophysical Research Letters*, 22, (22), 3031–3034, 1995.

Middlebrook, A. M. et al., Fourier transform-infrared studies of thin H_2SO_4/H_2O films: formation, water uptake and solid-liquid phase changes, *Journal of Geophysical Research: Atmospheres*, 98, (D11), 20473–20481, 1993.

Middlebrooks, A. M., M. A. Tolbert, and K. Drdla, Evaporation studies of model polar stratospheric cloud films, *Geophysical Research Letters*, 23, (16), 2145–2148, 1996.

Molina, M. J. et al., Physical chemistry of the $H_2SO_4/HNO_3/H_2O$ system: implications for the stratosphere, *Science*, 261, 1418–1423, 1993.

NASA, *Earth Atmosphere Model*, URL: `http://www.grc.nasa.gov/WWW/k-12/airplane/atmosmet.html`, June 30, 2010date.

Natsheh, A. A. et al., Coexistance of metastable nitric acid dihydrates: a molecular level contribution to understanding the formation of polar stratospheric cloud crystals, *Chemical Physics Letters*, 426, 20–25, 2006.

Peter, T. et al., The lifetime of lee wave-induced ice particles in the Artic stratosphere: II. Stabilization due to NAT-coating, *Geophysical Research Letters*, 21, (13), 1331–1334, 1994.

Pitts, M. C. et al., Characterization of Polar Stratospheric Clouds with spaceborne lidar: CALIPSO and and the 2006 Antarctic season, *Atmospheric Chemistry and Physics*, 7, 5207–5228, 2007.

Pitts, M. C., L. R. Poole, and L. W. Thomason, CALIPSO polar stratospheric cloud observations: second-generation algorithm and composition descrimination, *Atmospheric Chemistry and Physics*, 9, 7577–7589, 2009.

Pitts, M. C. et al., The 2009-2010 Arctic polar stratospheric cloud season: a CALIPSO perspective, *Atmospheric Chemistry and Physics*, 11, 2161–2177, 2011.

Pitts, M. C. et al., An assessment of CALIOP polar stratospheric cloud compostion classification, *Atmospheric Chemistry and Physics Discussions*, 12, 24643–24676, 2012.

Poole, L. R. and M. P. McCormick, Airborne lidar observation of Arctic polar stratospheric clouds: indications of two distinct growth stages, *Geophysical Research Letters*, 15, (1), 21–23, 1988.

Read, W. G. et al., EOS Aura Microwave Limb Sounder upper troposheric and lower stratospheric humidity validation, *Journal of Geophysical Research: Atmospheres*, 112, (D24S35), 2007.

Rienecker, M. M. et al., MERRA: NASA's Modern-Era Retrospective Analysis for Research and Applications, *Journal of Climate*, 24, 3624–3648, 2011.

Rolph, G. D. and R. R. Draxler, Sensitivity of 3-dimensional trajectories to the spatial and temporal densities of the wind field, *Journal of Applied Meteorology*, 29, 1043–1054, 1990.

Santee, M. L. et al., UARS Microwave Limb Sounder HNO_3 observations: implications for Antarctic polar stratosheric clouds, *Journal of Geophysical Research: Atmospheres*, 103, (D11), 13285–13313, 1998.

Santee, M. L. et al., Validation of the Aura Microwave Limb Sounder HNO_3 measurements, *Journal of Geophysical Research: Atmospheres*, 112, (D24S40), 2007.

Solomon, S. et al., On the depletion of Arctic ozone, *Nature*, 321, (6072), 755–758, 1986.

Steele, H. M. and P. Hamill, Effects of temperature and humidity on the growth and optical properties of sulphuric acid - water droplets in the stratoshpere, *Journal of Aerosol Science*, 12, (6), 517–528, 1981.

Stefanutti, L. et al., Polar stratospheric cloud observations over the Antarctic continent at Dumont d'Urville, *Journal of Geophysical Research: Atmospheres*, 96, 12975–12987, 1991.

Strawa, A. W. et al., Discriminating types 1a and 1b polar stratospheric clouds in POAM satellite data, *Journal of Geophysical Research: Atmospheres*, 107, (D20), 2002.

Svendsen, S. H. et al., Influence of mountain waves and NAT nucleation mechanisms on polar stratospheric cloud formation at local and synoptic scales during the 199-2000 Arctic winter, *Atmospheric Chemistry and Physics*, 5, 739–753, 2005.

Tabazadeh, A. et al., A study of type I polar stratospheric cloud formation, *Geophysical Research Letters*, 21, 1619–1622, 1994.

Tabazadeh, A. et al., Laboratory evidence for surface nucleation of solid polar stratospheric cloud particles, *Journal of Physical Chemistry A*, 106, 10238–10246, 2002.

Toon, G. C. et al., Infrared aircraft measurements of stratospheric composition over Antarctica during September 1987, *Journal of Geophysical Research: Atmospheres*, 94, (D14), 16571–16596, 1989.

Toon, O. B. et al., An analysis of lidar observations of polar stratospheric clouds, *Geophysical Research Letters*, 17, (4), 393–396, 1990.

Tsias, A. et al., Freezing of polar stratospheric clouds in orographically induced strong warming events, *Geophysical Research Letters*, 24, (18), 2303–2306, 1997.

Turco, R. P., O. B. Toon, and P. Hamill, Hetrogeneous Physicochemistry of the polar ozone hole, *Journal of Geophysical Research: Atmospheres*, 94, (D14), 16,493–16510, 1989.

WMO, *Scientific assessment of ozone depletion: 2010*, World Meteorological Organization Global Ozone Research and Monitoring Project Report No. 52, 2010.

Waters, J. W. et al., *An Overview of the EOS MLS Experiment*, Jet Propulsion Laboratory, California Institute of Technology, 2004.

Wofsy, S. C. et al., Condensation of HNO_3 on falling ice particles: mechanism for denitrification in the polar stratosphere, *Geophysical Research Letters*, 17, (4), 449–452, 1990.

Worsnop, D. R. et al., Vapor-pressures of solid hydrates of nitric-acid: implications for polar stratospheric clouds, *Science*, 259, (5091), 71–74, 1993.

Zhang, R. Y., M. T. Leu, and M. J. Molina, Formation of polar stratospheric clouds on preactivated background aerosols, *Geophysical Research Letters*, 23, (13), 1669–1672, 1996.

van Beek, T., *the color of the night*, URL: http://www.azimuthproject.org/azimuth/show/Blog+-+the+color+of+night, Jan. 7, 2012date.